Detection of transience in eroding landscapes

Detection of transience in eroding landscapes

Simon M. Mudd, University of Edinburgh, School of GeoSciences, Drummond Street, Edinburgh EH8 9XP, UK; simon.m.mudd@ed.ac.uk

KEYWORDS: Landscape evolution, transience, cosmogenic nuclides, tectonic geomorphology

Abstract

Past variations in climate and tectonics have led to spatially and temporally varying erosion rates across many landscapes. In this contribution I examine methods for detecting and quantifying the nature and timing of transience in eroding landscapes. At a single location, cosmogenic nuclides can detect the instantaneous removal of material or acceleration of erosion rates over millennial timescales using paired nuclides. Detection is possible only if one of the nuclides has a significantly shorter half-life than the other. Currently, the only practical way of doing this is to use cosmogenic in-situ ^{14}C alongside a longer lived nuclide, such as ^{10}Be. Hillslope information can complement or be used in lieu of cosmogenic information: in soil mantled landscapes, increased erosion rates can be detected for millennia after the increase by comparing relief and ridgetop curvature. This technique will work as long as the final erosion rate is greater than twice the initial rate. On a landscape scale, transience may be detected based upon disequilibria in channel profiles or ridgetops, but transience can be sensitive to the nature of transient forcing. Where forcing is periodic, landscapes display differing behavior if forcing is driven by changes in base level lowering rates versus changes in the efficiency of either channel or hillslope erosion (e.g. driven by climate change). Oscillations in base level lowering lead to basin averaged erosion rates that reflect a long term average erosion rate despite

24   strong spatial heterogeneity in local erosion rates. This averaging is reflected in [10]Be

25   concentrations in stream sediments. Changes in hillslope sediment transport coefficients

26   can lead to large fluctuations in basin averaged erosion rates, which again are reflected

27   in [10]Be concentrations. The variability of erosion rates in landscapes where both the

28   sediment transport and channel erodibility coefficients vary is dominated by changes to

29   the hillslope transport coefficient.

Introduction

31   Gone are the days when geomorphologists thought of landscapes as experiencing a

32   period of 'rejuvenation' followed by a dignified, if not dull, period of gradual adjustment

33   (c.f., Davis, 1899). We now understand the Earth's crust to be constantly in motion, with

34   faults rupturing and plates buckling under tectonic stresses, all leading to surface

35   deformation (e.g., Kirby and Whipple, 2010). In addition, there is now growing recognition

36   that the mantle also has a role to play, as large scale convection, mantle plumes and

37   diapirs are thought to lead to vertical displacements over geologic timescales (e.g.,

38   Rohrman and van der Beek, 1996; Saunders et al., 2007; Braun, 2010; Hartley *et al*.,

39   2011; Moucha and Forte, 2011). In addition, plutonism can lead to density differences

40   that drive uplift (e.g., Braun et al., 2011). Isotope records show beyond doubt that our

41   planet's climate varies wildly and sometimes abruptly, with ice sheets growing and

42   shrinking (e.g., Dansgaard *et al.*, 1993) and sea levels rising and falling by tens of meters

43   (e.g., Lambeck and Chappell, 2001).

44

45   Geodynamic and climatic activity plays a fundamental role in shaping our planet's

46   terrestrial surface. Geomorphologists have increasingly turned their attention to

47   quantifying the effects of tectonic and climatic change on rivers and hillslopes. In the last

48   few decades, new developments have led to intensified research into the nature and

49   speed of landscape adjustment. Several provocative physical experiments have

50   reproduced morphologies that resemble large catchments and even mountain ranges,

51   but that displayed unexpected landscape dynamism. The tank experiments of Hasbargen

52   and Paola (2000) and the sandboxes of Lague *et al.* (2003) and Bonnet *et al.* (2009)

53   featured landscapes that would equilibrate to a steady sediment flux rate. The flux rate in

54   these experiments was defined as the sediment removed from the system averaged over

55   the time necessary to erode through the highest point on the landscape. The geometry of

56   these experimental landscapes, however, was anything but steady. Divides moved,

57   knickpoints migrated and the organisation of the drainage network varied vigorously

58   through time.

59

60   Numerical modelling has also stimulated interest in the transient state of landscapes. Like

61   analogue experiments, numerical models have allowed workers to see virtual mountain

62   ranges grow and adjust to changing climate (as approximated by changing precipitation

63   and erodibility coefficients) and tectonics (as approximated by changing uplift rates or

64   lateral displacement). Many early models were constructed with the aim of predicting the

65   topographic outcome of so-called geomorphic transport laws (sensu Dietrich *et al.*, 2003).

66   This mirrored early analytical work by pioneers such as Culling (1960), who linked

67   constitutive equations linking sediment transport with topographic forms. Culling famously

68   showed why hilltops are convex, in an elegant mathematical demonstration of Gilbert's

69   (1909) earlier hypothesis. Whereas the early focus of many modelling studies was to

70   recreate digital topography that resembled natural topography, there has been a

71   movement in recent years to use models to test, or at least falsify, hypotheses about past

72   landscape evolution in the face of changing tectonic or environmental forcing.

73

74   One feature of early models was that an established drainage network and its ridge

75   network tended to stay in a fixed position (e.g., Howard, 1994). These results contrasted

76   with widespread observation of landforms interpreted to result from drainage capture

77   (e.g., Davis, 1889; Bishop, 1995), and also contrasted with experimental models. One

78   early model that did predict evolving drainage divides was that of Smith *et al.* (1997),

79   which predicted the splitting of divides, as observed in the tank experiments of Hasbargen

80   and Paola (2000). More recent models have tried to account for changing drainage areas

81   as hillslopes adjust to transient forcing, leading to models predicting a much more

82   dynamic drainage and ridgetop network (Pelletier, 2004; Castelltort *et al.*, 2012; Goren *et*

83   *al.*, 2014). Research based on recent metrics that detect disequilibrium across drainage

84   divides supports the widespread presence of highly dynamic landscapes, even in

85   tectonically quiescent settings such as the Appalachians (Willett *et al.*, 2014).

86

87   Within the context of changing tectonics and climate, and the potential complication of

88   autogenic landscape variability (e.g., Jerolmack and Paola, 2010; Coulthard and Van de

89   Wiel, 2013), one of the major challenges in geomorphology is to try to reconstruct past

90 changes based on current information (e.g., Wobus *et al*., 2010; Whittaker, 2012).

91 Geomorphologists can rarely work with a time series of landscapes: geomorphic change

92 may occur over thousands to millions of years and, barring the invention of time travel,

93 we will, in most cases, need to work with current landscape properties in order to

94 reconstruct past changes. However, there are a number of recent advances that may give

95 us some insight into how the landscape arrived at its current configuration.

96

97 Two advances that have refreshed the study of geomorphology are the measurement

98 and interpretation of cosmogenic radionuclides (CRNs; e.g., Bierman *et al*., 1994) and

99 the rapid expansion of the quality and availability of high resolution topographic data (e.g.,

100 Slatton *et al*., 2007). While the application of CRNs to geomorphic research is now

101 considered mature, improving instrument sensitivity and analytical techniques are

102 extending the range of application (Rood *et al*., 2010). New measurement techniques,

103 notably for in-situ cosmogenic ^{14}C, are opening opportunities for querying landscapes.

104 In-situ cosmogenic ^{14}C has only been measured reliably in laboratories in the last 5 years

105 (e.g., Fulop *et al*., 2010; Hippe *et al*., 2013; Goehring *et al*., 2014) but offers new

106 opportunities to examine landscape transience.

107

108 High resolution topography, primarily generated using airborne light detection and ranging

109 (lidar), has allowed us to quantify topography on sub-meter scale. It is not unusual for

110 modern airborne lidar campaigns to collect dozens, or even hundreds of square

111 kilometres at point cloud densities of >10 pts m^{-2}. This presents unprecedented

112   opportunities for geomorphologists and ecologists alike (e.g., Tarolli, 2014; Passalacqua

113   *et al.,* 2015): not only do these data allow sensing of the plant canopy (e.g., Dubayah and

114   Drake, 2000; Lefsky *et al.*, 2002), but they also allow geomorphologists to observe and

115   quantify landscape features at the process scale, such as evidence of biotic activity (e.g.,

116   Roering *et al.*, 2010; Gabet *et al.*, 2014), fault scarps (e.g., Sherrod *et al.*, 2004;

117   Arrowsmith and Zielke, 2009), headwater channels (e.g., Passalacqua *et al.*, 2010;

118   Orlandini *et al.*, 2011; Pelletier, 2013; Clubb *et al.*, 2014), bedrock outcrop (e.g. DiBiase

119   et al., 2012; Milodowski et al., 2015) and other relevant features.

120

121   While sedimentary archives may be used to detect landscape transience (e.g., Schaller

122   et al., 2002; Balco and Stone, 2005; Armitage et al., 2011; Charreau et al., 2011; Marshall

123   et al., 2015), I wish to focus here on eroding landscapes where sediment export precludes

124   the use of such archives to detect transience. In this contribution I aim to show that

125   landscape transience may be both detected and quantified in the absence of sedimentary

126   deposits using topography and cosmogenic nuclides.

Detection of change in a single soil profile using in-situ cosmogenic nuclides

129

130   One of the most revolutionary developments in the last 30 years in geomorphology is the

131   widespread adoption of methods based on in-situ cosmogenic radionuclides (CRNs);

132   since the seminal work of Lal (1991), hundreds of authors have used the concentration

133   of CRNs to infer past erosion rates. Applications of CRNs in geomorphic studies

134   frequently use an assumption that erosion rates are constant in time (a review of the many

135   applications can be found in Dunai, 2010 and Granger *et al.*, 2013), but fewer authors

136   have sought to examine how CRN concentrations may be used in transient settings.

137   Several authors have examined how CRN concentrations may be expected to vary in

138   soils in the face of either periodic (e.g., Heimsath, 2006) or stochastic (Lal, 1991; Small

139   *et al.*, 1999; Musikar, 2009; Parker and Perg, 2005; Heimsath, 2006; Schaller and Ehlers,

140   2006) variations in erosion rates. A key concept in these studies is that the concentration

141   of CRNs can be inverted for an erosion rate. This erosion rate is 'apparent' because it

142   depends on the assumptions used in the inversion and may not reflect the actual erosion

143   rate. For example, an apparent erosion rate may be calculated using Lal's (1991)

144   equation for steady state erosion, but this equation assumes erosion rates and

145   cosmogenic production rates that do not vary in time. This contrasts with the actual

146   erosion rate, by which I mean the erosion rate that has actually occurred, or in other words

147   the amount of material removed divided by the time over which this removal is averaged,

148   and in addition the apparent erosion rate may not reflect the instantaneous erosion rate,

149   i.e., the erosion rate that is currently occurring in the landscape.

150

151   One of the key findings of studies investigating the effect of transient erosion rates on

152   CRN concentrations is that the apparent erosion rates derived from CRN concentrations

153   will reflect the time integrated erosion rate. In addition the lag between instantaneous and

154   apparent erosion rates will increase with greater amplitude variations in erosion rate and

155   shorter periods of periodic forcing or time between stochastic events. Alternatively, low

156   frequency variations in erosion rate and low amplitude variations in erosion rate will result

157   in apparent erosion rates that more closely reflect the instantaneous erosion rate.

158

159   The focus of most studies examining the effect of erosion transience has focused on the

160   accuracy of inferred erosion rates in the face of erosion variability, but few have

161   commented on using CRN concentrations to infer past changes in erosion rates. Lal

162   (1991) famously constructed plots of the ratio between [10]Be and [26]Al concentration

163   against [10]Be concentration to demonstrate the existence of a 'steady state island' in this

164   parameter space: samples plotting outside this steady state island had a more complex

165   erosion and exposure history. This principle is used extensively in the dating of surfaces

166   and burial dating (e.g., Granger 2006). In eroding landscapes, however, we can narrow

167   the range of exposure histories since it is a reasonable assumption that on sloping

168   ground, material is continuously eroding and unlikely to experience prolonged periods of

169   exposure or burial. With these constraints in mind, I would like to examine the possibility

170   of inferring past erosional changes in eroding landscapes using CRN concentrations.

171

172   I begin with a general statement of conservation of a nuclide for a steadily eroding surface

173   (e.g., Granger and Smith, 2000, Schaller *et al.*, 2002; Vermeesch, 2007):

174

$$C_i = C_{i,0}\, e^{(t-t_0)\lambda_i} + P_{i,SLHL} S_{tp} \sum_{j=0}^{n} \left[\frac{S_j F_{i,j} \Gamma_{i,j}}{\varepsilon - \Gamma_{i,j}\lambda_i} e^{-(d+\varepsilon t)/\Gamma_{i,j}} \left(e^{(t-t_0)\varepsilon/\Gamma_{i,j}} - e^{(t-t_0)\lambda_i} \right) \right], \qquad (1)$$

175

176   where C_i is the concentration of nuclide i, $C_{i,0}$ (typically reported in atoms per gram) is the

177   initial concentration of this nuclide, t and t_0 are the current and initial time, respectively, λ_i

178   is the decay coefficient (T^{-1}, dimensions henceforth denoted in [M]ass, [L]ength, and

179   [T]ime in square brackets), $P_{i,SLHL}$ is the production rate of nuclide i at sea level and high

180   latitude (in units atoms g^{-1} yr^{-1}), S_{tp} is a dimensionless scaling factor due to topographic

181   shielding, the subscript j refers to the production mechanism (this could be either

182   nucleonic spallation or various muogenic pathways), S_j is a dimensionless scaling factor

183   that accounts for a number of effects such as changing production rates as a function of

184   altitude or pressure, shielding from snow and self-shielding (e.g., Vermeesch, 2007), $F_{i,j}$

185   is a dimensionless factor that determines the proportion of nuclide production due to each

186   mechanism, $\Gamma_{i,j}$ [M L^{-2}] is the attenuation length (typically reported in g cm^{-2}), ε is erosion

187   rate in mass equivalent units (typically g cm^{-2} yr^{-1}) and d is a mass per unit area that is

188   related to the depth by:

189

$$d = \int_{\zeta-h}^{\zeta} \rho(z)dz,$$

(2)

190

191   where ζ [L] is the elevation of the surface, h [L] is depth below the surface, and ρ [M L^{-3}]

192   is the density of the rock or regolith as a function of elevation. The quantity d is called the

193   shielding depth.

194

195   Results of experiments conducted by Heisinger *et al*. (2002a, b) suggested that muons

196   could contribute significantly to CRN production at depth, but measurements from field

197   sites now suggest that production from muons is smaller than suggested by experiments

198   (Braucher *et al*., 2013); for example Braucher *et al*. (2013) reported that muogenic

199   production of ^{10}Be accounted from ~0.5% of the total production, with the remainder

200   produced by nucleonic spallation. With only nucleonic spallation, equation (1) reduces

201   to:

202

$$C_i = C_{i,0}\, e^{(t-t_0)\lambda_i} + P_{i,SLHL} S_t \left[e^{-(d+\varepsilon t)/\Gamma} \left(e^{(t-t_0)\varepsilon/\Gamma} - e^{(t-t_0)\lambda_i} \right) \right], \qquad (3)$$

203

204   where S_t [dimensionless] is a combined scaling term that takes into account production

205   scaling and snow, self and topographic shielding.

206

207   Equation (3) may be solved for the steady state concentration if *t* approaches infinity and

208   the initial concentration is zero (e.g., Lal, 1991):

209

$$C_{i,SS} = \frac{P_{i,SLHL} S_t \Gamma}{\varepsilon + \Gamma \lambda_i} e^{-\frac{d}{\Gamma}}. \qquad (4)$$

210

211   Equation (4) can then be solved for the apparent erosion rate, ε_{app} (in units g cm^{-2} yr^{-1}),

212   which one would infer from CRN concentration if the system were assumed to be in

213   steady state:

214

$$\varepsilon_{app} = \frac{e^{-\frac{d}{\Gamma}}P_{i,SLHL}S_t\Gamma - C_i\Gamma\lambda_i}{C_i}. \tag{5}$$

215

216   My aim is to exploit equations (3-5) to gain information about past erosion rates, focusing

217   on two scenarios.

218

Scenario 1: Instantaneous removal of mass

219
220

221   The first scenario is one in which there is a constant background erosion rate but some

222   thickness of material is removed instantaneously from the surface. This scenario mimics

223   a landslide, or alternatively is an approximation for a period of intense soil loss such as

224   that experienced in ancient Greece (e.g., van Andel *et al.*, 1990) or Rome (e.g., Judson,

225   1968), and builds on a similar analysis in Lal (1991).

226

227   The initial time, t_0, is set to zero and represents the moment the mass is removed (this

228   could be either bedrock or soil or a combination of the two, as long as mass removal is

229   instantaneous). The time t represents the time since mass removal. The initial

230   concentration of the nuclide will be determined by the steady state concentration

231   (equation 4), but the depth must be adjusted to account for removal of mass, such that

232   the adjusted depth, $d_{adj} = d + \varepsilon\,t + d_{br}$, where d_{br} is the depth of mass removal. This can

233   be inserted into equation (4), which can be substituted in as the initial concentration in

234   equation (3), and this concentration can be inserted into equation (5) to yield the apparent

235   erosion rate after mass removal:

236

$$\varepsilon_{app,br} = \left[\varepsilon\, e^{\frac{d_{br}+t\varepsilon+t\Gamma\lambda_i}{\Gamma}} + \Gamma\lambda_i\left(e^{\frac{d_{br}}{\Gamma}} - 1\right)\right]\left[1 + e^{d_{br}/\Gamma}\left(e^{t\left[\frac{\varepsilon}{\Gamma}+\lambda_i\right]} - 1\right)\right]^{-1}. \qquad (6)$$

237

238   It is perhaps useful here to explain how equations (3-6) might be practically applied.

239   Consider a situation in which the worker has no information about past changes in erosion

240   rates (i.e., there is no lake sediment record downstream, no historic erosion rate data,

241   etc.). The goal then is to use only the concentration of nuclides to determine past

242   transience. If erosion rates are constant in time, the apparent erosion derived from

243   equation (5) will be equal to the true erosion rate. However, if erosion rates are transient,

244   nuclide concentrations will reflect some averaging of past erosion. I seek a way to

245   diagnose if there has been transience by either quantifying changes in nuclide

246   concentrations with depth or quantifying differences between concentrations of different

247   nuclides. Equation (6) predicts an apparent erosion rate (that is, the erosion rate one

248   calculates assuming steady erosion) if nuclide concentrations are the result of mass

249   removal. That is, equation (6) is used to explore if nuclide concentrations at different

250   depths or from different nuclides report the same apparent erosion rate (in which case

251   the hypothesis that erosion is steady cannot be rejected) or if they report different

252   apparent erosion rates.

253

254   Inspection of equation (6) yields a significant result: the apparent erosion rate is not a

255   function of depth. This means that after mass removal, regardless of where in the soil or

256   regolith column samples are extracted, the apparent erosion rate is the same. This is

257   important because it means that the depth profile of a single CRN is of no use in

258   identifying landscape transience under the mass removal scenario.

259

260   If a single nuclide cannot reveal information about transience, what options are available

261   to detect transience? I will show below that a single nuclide also fails to provide

262   information about transience in the second scenario, featuring a step change in erosion

263   rate. All is not lost, however. Nuclides with differing decay coefficients equilibrate to local

264   conditions at different rates; this is the principle behind the steady state island plots of Lal

265   (1991) and various burial dating techniques (e.g., Granger *et al.*, 2012). For both

266   scenarios, the differing apparent erosion rates derived from two nuclides can be used to

267   reveal information about landscape transience.

268

269

270

271   Nuclides that decay more rapidly will adjust more quickly to changes in erosion rate (Lal,

272   1991). Thus, if mass is instantaneously is removed from the surface, the nuclide with

273   more rapid decay will have a greater perturbation to its apparent erosion rate. Following

274   Lal's (1991) lead, we may look for greater apparent erosion rates in shorter lived nuclides

275   to detect changes in erosion rates. I will thus compare $\varepsilon_{app,br}$ for two different nuclides

276   calculated using equation (6), as a function of the background erosion rate (ε), the depth

277   of the mass removal (d_{br}) and the time since mass removal (t).

278

279   To be conservative, I assume that any apparent erosion rate has 10% uncertainties

280   attached. Thus, to plausibly detect transience, the ratio between the two nuclides must

281   be greater than 20%. Note that in some cases, production rate uncertainties exceed this

282   value (e.g., Balco *et al.*, 2008), but in these examples the samples will have the same

283   production rate (since we are sampling effectively the same particle) so production

284   uncertainties will result in absolute but not relative uncertainties. We can also consider a

285   plausible range of background erosion rates. Erosion rates greater than 1 mm yr^{-1} are

286   widely considered to be rapid; this equates to ~0.25 g cm^2 yr^{-1} of bedrock lowering for

287   typical rock densities (~ 2.5 g cm^{-3}). There are landscapes with faster erosion rates but,

288   as we will momentarily see, even background erosion rates of 1 mm yr^{-1} are beyond our

289   current analytical limits for detecting transience. The lower limit of erosion is of course

290   zero, but the vast majority of sloping terrains (even ones located on very low relief cratons)

291   are eroding faster than 0.001 mm yr^{-1} (e.g., Portenga and Bierman, 2011, although bare

292   rock surfaces tend to erode more slowly; see their Figure 2a).

293

294 First, consider two commonly measured nuclides, ^{10}Be and ^{26}Al. These have decay

295 coefficients of $500*10^{-9}$ yr^{-1} (Chmeleff et al., 2010; Korschinek et al., 2010) and $980*10^{-9}$

296 yr^{-1} (Nishiizumi, 2004), respectively, and both have a value of 160 g cm^{-2} (Balco et al.,

297 2008). Even in a slowly eroding landscape (0.0026 g cm^{-2} yr^{-1}, equivalent to 0.01 mm yr^{-}

298 ^{1} in material with density 2.6 g cm^{-3}) where 500 g cm^{-2} of material is removed (this is

299 roughly equivalent to a ~2 m thick layer of bedrock) and the surface is sampled one year

300 after block removal, the difference in the apparent erosion rates is only 2% (ε_{app} for ^{10}Be

301 = 0.064 g cm^{-2} yr^{-1} versus ε_{app} for ^{26}Al = 0.062 g cm^{-2} yr^{-1}). The difference gets yet smaller

302 for thinner blocks and faster background erosion rates. Thus, it is virtually impossible to

303 detect removal of a block in an eroding landscape using paired ^{10}Be and ^{26}Al. In addition,

304 apparent erosion rates from stable nuclides (e.g., ^{21}Ne) cannot be differentiated from

305 apparent erosion rates derived from ^{10}Be and ^{26}Al.

306

307 Now, consider ^{10}Be and in-situ ^{14}C (λ = 1.21 x 10^{-4} yr^{-1}, Bowman, 1990). Several

308 laboratories are now capable of measuring cosmogenic in-situ ^{14}C (Fulop *et al.*, 2010;

309 Hippe et al, 2013; Goehring *et al.*, 2014), which is a promising nuclide due to its short

310 half-life, as I will demonstrate.   We can plot the ratio of apparent erosion rates for these

311 two nuclides after block removal, this is shown for two different background erosion rates

312 and two block removal depths in Figure 1. When 50 g cm^{-2} is removed, it can be detected

313 given our conservative threshold of a 20% difference for background erosion rates of

314 0.026 g cm^{-2} yr^{-1}, which is an approximate bedrock erosion rate of ~0.1 mm yr^{-1} (Figure

315   1a). At these rates, a mass removal of 50 g cm^{-2} can be detected for approximately 100

316   years after the mass removal. If the background erosion rate is slower, change can be

317   detected for thousands of years. If a mass of 150 g cm^{-2} is removed, one can detect this

318   removal for a millennium if background erosion rates are 0.026 g cm^{-2} yr^{-1} or slower

319   (Figure 1b). If background erosion rates are too rapid, however, mass removal cannot be

320   detected; with background erosion rates of 0.26 g cm^{-2} yr^{-1}, no thickness of mass removal

321   results in apparent erosion rates between ^{10}Be and ^{14}C exceeding the threshold of 20%

322   erosion rate difference. This method can therefore mass block removal in slowly eroding

323   landscapes, but the nuclide ratios are not unique: we should be able to tell if mass removal

324   has occurred but we cannot know both the time and depth of removal.

325

326   **Scenario 2: Step change in erosion rate**
327

328   The second scenario that I investigate is a situation where there has been a step change

329   in the erosion rate, from ε_{old} to ε_{new}. The initial concentration is determined by equation

330   (4). This concentration is then inserted into equation (2), and solved for the apparent

331   erosion rate, resulting in:

332

$$\varepsilon_{app,sc} = \left[\Gamma \lambda_i (\varepsilon_{old} - \varepsilon_{new}) \right.$$

$$+ \left. \varepsilon_{new} \, e^{t\left[\frac{\varepsilon_{new}}{\Gamma} + \lambda_i\right]} (\varepsilon_{old} + \Gamma \lambda_i) \right] \left[\varepsilon_{new} + \varepsilon_{old} \left(e^{t\left[\frac{\varepsilon_{new}}{\Gamma} + \lambda_i\right]} - 1 \right) \right.$$

$$+ \left. \Gamma \lambda_i e^{t\left[\frac{\varepsilon_{new}}{\Gamma} + \lambda_i\right]} \right]^{-1}. \tag{7}$$

333

334   Similar to equation (6), equation (7) is not a function of depth: one cannot use the depth

335   profile of a single nuclide to distinguish between a steady state profile and one that has

336   experienced a step change in erosion rate. Again, multiple nuclides must be used to

337   identify a site that has experienced a change in erosion rates; I explore the sensitivity of

338   a two-nuclide system as a function of the old and new erosion rates and the time since

339   the change in erosion rate (t).

340

341   As in the case of block removal, apparent erosion rates derived from [10]Be and [26]Al are

342   not sufficiently different to allow identification of transient erosion rates. In addition,

343   apparent erosion rates from stable nuclides (e.g., [21]Ne) cannot be differentiated from

344   apparent erosion rates derived from [10]Be and [26]Al. Even if erosion rates increase by a

345   factor of 10 in a slowly eroding landscape, the difference between apparent erosion rates

346   inferred from these two nuclides never exceeds 5%. To gain some insight into transient

347   processes we must use a nuclide pair with a greater difference in decay rates, so once

348   again I turn to [10]Be and in-situ [14]C.

349

350   First, we can examine the effect of acceleration in erosion rate (Figure 2a). Again I invoke

351   a conservative detection threshold of >20% difference in the apparent erosion rates

352   inferred from in-situ ^{10}Be and ^{14}C concentrations. A doubling of erosion rate is detectable

353   using the ^{10}Be and ^{14}C pair for an initial erosion rate of 0.0026 g cm^{-2} yr^{-1} between 500

354   and 2000 years after the acceleration.   Doubling of the erosion rate is not detectable if

355   the original erosion rate is 0.026 g cm^{-2} yr^{-1}. This implies that a doubling of erosion rate is

356   only detectable at very slow background erosion rates. On the other hand, a five times

357   acceleration in erosion rate is detectable with original erosion rates at both 0.0026 g cm^{-}

358   ^{2} yr^{-1} and 0.026 g cm^{-2} yr^{-1}, with the former being detectable after ~400 years and the

359   latter being detectable after ~2000 years (Figure 2a).

360

361   Similar detection limits are found if erosion rate decreases; in this case, the apparent

362   erosion rate inferred from ^{14}C is lower than that of ^{10}Be (Figure 2b). The major difference

363   between acceleration and deceleration in erosion is that if erosion rates decrease, they

364   cannot be detected for a long time (compared to accelerated erosion); for an erosion rate

365   of 0.0026 g cm^{-2} yr^{-1} and a reduction in the erosion rate by a factor of 5, one must wait

366   ~2000 years before transience can be detected using the ^{10}Be and ^{14}C pair.

367

368   Unfortunately, because of the self-similarity of CRN depth profiles, one cannot

369   differentiate between block removal and a step change with a depth profile, nor can one

370   uniquely find both the timing of acceleration or removal, so these techniques are limited

371   to detecting if a perturbation has occurred to the erosion rate in the past, and it can

372   constrain the upper limit of how long ago this perturbation occurred. CRNs, however, are

373   not the only means of detecting transience within the geomorphologist's toolkit.

374

Detection of hillslope transience from topography

376   In many cases, one might wish to look for evidence of landscape transience across

377   multiple hillslopes. One strategy is to look for a transition between low relief and high relief

378   surfaces, which may be interpreted as separating slowly eroding from rapidly eroding

379   portions of the landscape (e.g., Schoenbohm *et al.*, 2004; Gallen *et al.*, 2011; Anderson

380   *et al.*, 2012; Prince and Spotila, 2013). If changes in hillslope erosion rates are driven by

381   the propagation of knickpoints up the channel network, one might expect to find a pattern

382   of hillslope disturbance in which the proportion of the hillslope affected by the greater

383   erosion rate increases downstream of the channel knickpoint (e.g., Mudd and Furbish,

384   2007; Hurst *et al.*, 2012). Differentiating zones of rapid erosion from zones of slow erosion

385   on a hillslope is not always trivial. In some cases a clear break in slope is visible (e.g.,

386   Rheinhardt *et al.*, 2007), but in many cases a change along a profile is difficult to quantify

387   since hillslopes, even at steady state, will have gradients that increase downhill (e.g.,

388   Culling, 1960). In addition, in most rapidly eroding landscapes, hillslopes tend to approach

389   a critical slope angle (e.g., Roering *et al.*, 2001; Binnie *et al.*, 2007; DiBiase *et al.*, 2010)

390   and thus at high erosion rates, hillslope gradients become insensitive to erosion rates.

391

392 An alternative to searching for a break in slope is to use the relief structure in the

393 landscape, in combination with information about ridgetops, to detect landscape

394 transience. Roering *et al.*, (1999) observed that in rapidly eroding landscapes in the

395 Oregon Coast Range, soil-mantled hillslopes tended to become planar away from hilltops;

396 this topography was consistent with a sediment flux law that predicted as hillslope

397 gradients approached a critical slope, S_c [dimensionless], sediment flux (q_s [L^2 T^{-1}]) would

398 rapidly increase. This flux law mirrored one earlier proposed by Andrews and Bucknam

399 (1987):

400

$$\vec{q}_s = -\frac{D\,\nabla\zeta}{1-\left(\frac{|\nabla\zeta|}{S_c}\right)^2}, \tag{8}$$

401

402 where D [L^2 T^{-1}] is a sediment transport coefficient and the arrow indicates that sediment

403 flux is a vector quantity (also recall ζ denotes surface elevation). Combining this flux law

404 with a statement of mass conservation, Roering *et al.* (2007) noted that on ridgetops,

405 where topographic gradients are low, erosion rates should be linearly proportional to

406 ridgetop curvature, C_{HT} [L^{-1}] (that is, the second derivative of surface topography, $\nabla^2\zeta$) in

407 steadily eroding landscapes. In addition, Roering *et al.* (2007) found the steady solution

408 of surface topography in one dimension, and were able to demonstrate that all steadily

409 denuding hillslopes obeying equation (8) should fall on the nondimensional curve,

410

$$R^* = \frac{1}{E^*}\left[\sqrt{1 + (E^*)^2} - ln\left(\frac{1}{2}\left[1 + \sqrt{1 + (E^*)^2}\right]\right) - 1\right], \tag{9}$$

411

412   where

413

$$R^* = \frac{R}{S_c L_H}, \tag{10}$$

414

415   and

416

$$E^* = \frac{2(\rho_r/\rho_s)L_H}{DS_c} = -\frac{2C_{HT}L_H}{S_c}. \tag{11}$$

417

418   The quantity R^* is a dimensionless relief: it is the relief (R [L]) from channel to ridgetop

419   scaled by the critical slope S_c and the hillslope length L_H. The density subscripts r and s

420   refer to rock and soil densities, respectively. It can also be interpreted as the mean

421   topographic gradient of the hillslope divided by the critical slope. The quantity E^* is a

422   dimensionless erosion rate. Roering *et al.* (2007) went on to demonstrate that sites in the

423   Oregon Coast Range and Gabilan Mesa, California, plot in E^* vs R^* space along the curve

424   predicted by equation (9). Hurst *et al.* (2012) showed that in a landscape in the Northern

425   Sierra Nevada of California, ridgetop curvature was linearly proportional to erosion rate

426   and that, across the range of erosion rates in the study area (0.01 to 0.25 mm yr^{-1}), the

427   *E** vs *R** values plotted, within error, on the curve described by equation (9). This suggests

428   equation (8) is consistent with the topography of these landscapes, corroborating the

429   findings of Roering *et al.* (1999), Roering (2008) and Grieve et al. (2016).

430

431   What happens, then, if channel incision rates change? We do have some idea of how

432   long it takes for hillslopes to adjust to changes in channel incision rates. One measure of

433   the time it takes a hillslope to adjust to changing channel incision rates is a hillslope's

434   relaxation time, a concept borrowed from the physics of heat diffusion (e.g., Carslaw and

435   Jaeger, 1959). The relaxation time measures the time a diffusion-like system (such as

436   molecular diffusion, diffusion of thermal energy, diffusion of pore pressure within

437   saturated groundwater systems, or the diffusion-like behavior of surface elevation on

438   creep-dominated hillslopes) equilibrates to a steady state after a perturbation. The formal

439   definition of the relaxation time is the time it takes a system under steady forcing, e.g., a

440   hillslope with a steadily eroding channel at its base, to return to within e^{-1} (which is

441   approximately 0.37) of the steady condition (in the hillslope case measured by erosion

442   rate). For example, if a hillslope was eroding at 1 mm yr^{-1} and the channel then began

443   eroding at 2 mm yr^{-1}, the relaxation time would be the time required for the average

444   hillslope erosion rate to reach 1.63 mm yr^{-1}.

445

446 Fernandes and Dietrich (1997) used numerical simulations to show that for hillslopes

447 where $q_s = -D\rho_s S$, where S is the topographic gradient, the relaxation time is proportional

448 to L_H^2/D, although they used a threshold of 90% of the steady erosion rather than the e-

449 folding timescale to define the relaxation time. Mudd and Furbish (2007) later showed

450 through analytical solution that the formal relaxation time is exactly $4L_H^2/(D\pi^2)$. The

451 relaxation time can be reduced in landscapes where sediment flux is nonlinearly

452 proportional to topographic gradient (e.g., Roering *et al.*, 2001) or is proportional to the

453 product of gradient and soil thickness (e.g., Mudd and Furbish, 2007) relative to

454 landscapes where sediment flux is linearly proportional to topographic gradient. In

455 general, the relaxation time is strongly related to hillslope length and the sediment

456 transport coefficient.

457

458 Now consider the following scenario. Imagine a wave of channel incision passes the base

459 of a hillslope. The time it takes for a signal of channel incision to reach the hilltop is a

460 function of the flux law: Mudd and Furbish (2007) showed that it takes 1/9 of the relaxation

461 time for the hilltop to be affected after channel perturbation where sediment flux is linearly

462 proportional to slope; nonlinear slopes such as those described by equation (8) can

463 respond yet more quickly (Roering *et al.*, 2001). In both cases, however, there is a delay

464 between increased channel incision and any response of the hilltop. The result of this

465 delay is that hilltop curvature will lag behind hillslope relief in a transient landscape. One

466 can calculate an apparent E^* value for a hilltop, regardless of whether it is at steady state

467 or not: $E^*_{app} = 2C_{HT} L_H /S_c$. If the channel incision rate has increased, the hilltop-based

468 apparent dimensionless erosion rate (E^*_{app}) should be less than that predicted by the

469   steady state curve described by equation (9) for a given dimensionless relief, $R*$ (Figure

470   3), since the hilltop will not yet have adjusted to the new erosion rate. If channel incision

471   rates decrease, $E*_{app}$ will be greater than the $E*$ predicted by the steady state curve. Thus,

472   increases and decreases in channel incision rates can be detected by hillslopes lying

473   above and below the steady state curve in $E*$ vs $R*$ space, respectively (Hurst et al.,

474   2013a; Figure 3).

475

476   Hurst *et al.* (2013a) tested this hypothesis along the Dragon's Back Pressure Ridge, a

477   landform that lies along the San Andreas Fault (SAF) in California. It is the result of

478   deformation and uplift caused by the fault motion advecting the local sedimentary

479   formation (the Paso Robles formation, made of weakly consolidated sediments) over an

480   offset in the SAF that remains stationary in relation to the North American Plate (Hilley

481   and Arrowsmith 2008). Detailed field mapping and palinspastic reconstruction of the

482   deformed beds by Hilley and Arrowsmith (2008) has resulted in a uniquely well-

483   constrained uplift field. Due to the motion of the fault, small catchments running

484   perpendicular to the fault pass over and then away from this uplift field such that it is

485   possible to quantify a space for time substitution on changing basin uplift as a function of

486   position along the pressure ridge (Hilley and Arrowsmith 2008).

487

488   Hurst *et al.* (2013a) found that catchments that had recently passed over the zone of

489   maximum uplift plotted above the steady state curve described by equation (9), and as

490   catchments moved away from the zone of uplift their hillslopes adjusted towards the

491   steady-state line by increasing their E^*_{app} before relief declined taking them below the

492   steady state curve. This exposition of topographic hysteresis demonstrated the utility of

493   comparing hillslope relief to hilltop curvature in order to identify landscapes that are

494   growing from those that are static or waning.

495

496   These results beg the question: just how much of an increase or decrease in channel

497   incision is required for transience to be detected using the E^* vs R^* technique? Using the

498   one dimensional model of Hurst *et al.* (2013a), I have explored both the magnitude and

499   timing of a hillslope's departure from the steady state E^* vs R^* curve for different initial

500   and final channel erosion rates. The model starts from a steady state hillslope profile, and

501   then channel incision undergoes a step change.

502

503   Figure (4a) shows the maximum difference in dimensionless relief that is measured on

504   the hillslope and that is predicted by equation (9) as the hillslope responds to a change in

505   channel incision. As a point of reference, the standard errors in observed R^* values from

506   the Dragon's Back Pressure Ridge (DBPR) reported by Hurst *et al.* (2013a) are plotted:

507   these errors are due to the natural variability in relief along the DBPR ridgelines.

508   Differences in measured and predicted R^* that are less than this error cannot be resolved,

509   so this gives some indication of how great a perturbation in incision rate is required before

510   changes in R^* can be resolved. This error is not universal: each landscape will have its

511   own variability in ridgeline relief (e.g., Gabet et al., 2015); the DBPR errors are plotted

512   simply as a point of reference. Figure (4a) indicates that reductions in channel incision

513 are more difficult to resolve than landscapes where channel incision rates have increased.

514 In addition, it is easier to resolve landscape transience if the initial channel incision rate

515 is greater, which is somewhat counterintuitive. The reason for this is that a doubling of

516 erosion rate from initially low erosion does not lead to as large of an increase in R^*.

517

518 For relatively fast initial channel incision rates, a doubling of the channel incision rate

519 should be resolvable from the difference between predicted and measured R^*. For

520 parameter values of $\rho_r/\rho_s = 2$, $D = 0.01$ m^2 yr^{-1}, $L_H = 25$ m and $S_c = 1$ (these are values

521 similar to DBPR), an E^* of 1 equates to an incision rate of 0.4 mm yr^{-1}, an erosion rate

522 that is frequently achieved in tectonically active landscapes (see, for example, the erosion

523 rate compilation of Portenga and Bierman, 2011).

524

525 Figure (4b) shows the time needed to reach the maximum difference between measured

526 and predicted R^*, in units of dimensionless time, t^*. Time is scaled by $t^* = (D/L_H^2)\, t,$ where

527 t is dimensional time. The time required to reach the maximum difference in measured

528 and predicted R^* varies between approximately $t^* = 0.01$ and $t^* = 0.1$ after the

529 perturbation. This result should not come as a surprise because t^* is scaled by a time

530 similar to the relaxation time; Mudd and Furbish (2007) showed that it takes approximately

531 1/9 of the relaxation time for a change in channel incision to reach the divide. For $D =$

532 0.01 m^2 yr^{-1} and $L_H = 25$ m, $t^* = 0.1$ equates to 6250 years. This suggests that in rapidly

533 eroding landscapes, the E^* vs R^* method could be used to identify changes in channel

534   incision, perhaps brought about by changing tectonic activity, that has occurred in the last

535   few millennia.

536

How reliable is the assumption of constant transport coefficients in the face of varying climate?

537
538
539

540   In the previous section, the models used to quantify landscape transience based on

541   topographic data and other landscape features relied on an assumption that the sediment

542   transport coefficient, D, could be independently quantified. A number of strategies have

543   been used to calculate the transport coefficient. Two commonly used techniques for

544   calculating D are: i) to compare measurements of flux against topographic gradients (e.g.,

545   McKean *et al.*, 1993; Heimsath *et al.* 2005; Jungers *et al.*, 2009) or ii) to compare long

546   term erosion rates to topography (e.g., Roering *et al.*, 1999; Heimsath *et al.* 1999; Small

547   *et al.* 1999; Roering, 2008, Riggins *et al.*, 2011; Hurst *et al.*, 2012). Often these methods

548   rely on fluxes or erosion rates derived from in-situ cosmogenic nuclides, which average

549   erosion rates over thousands of years. In addition, topography also evolves over

550   millennia. A critical question therefore is this: if the sediment transport coefficient has

551   changed due to, for example, climate induced vegetation changes, what then does the

552   transport coefficient inferred from today's topography represent?

553

554   I attempt to constrain the meaning of a topographically derived transport coefficient by

555   running simulations that involve a step change in the transport coefficient, D. The

556 analogue for this step change is the case of a landscape that experiences a vegetation

557 shift, for example from grassland to forest (e.g., Roering *et al.*, 2004; Hughes *et al.*, 2009).

558 The hillslope evolves based on the nonlinear sediment flux law described by equation (9);

559 the numerical implementation is the same as that of Hurst *et al.* (2013a). In addition, the

560 concentration of ^{10}Be being removed from the hilltop is calculated using equation (3). This

561 concentration is inserted into equation (5), yielding the apparent erosion rate, i.e. the

562 erosion rate one would calculate if one assumed steady erosion. An apparent sediment

563 transport coefficient is then calculated using the relationship (Hurst *et al.*, 2012):

564

$$D_{app} = -\frac{\varepsilon_{app}}{C_{HT}}\frac{\rho_r}{\rho_s}. \qquad (12)$$

565

566 The error in the transport coefficient, *D*, is then calculated as a function of time since the

567 step change. These errors are plotted in Figure 5. Immediately after the step change in

568 *D,* errors are large because topography reflects the old transport coefficient. As time

569 passes, however, topography adjusts to the new transport coefficient until errors are

570 small.

571

572 We can examine Figure 5 in the context of estimating *D* at a field site. How much time

573 must elapse after a change in *D* so that the estimate of *D*, calculated using CRN-derived

574 erosion rates and topographic curvature, is a reasonable approximation for the current

575   value of D in the landscape? In Figure 5, the time is scaled by dimensionless time, t^* (see

576   previous section), which is calculated based on the transport coefficient after its step

577   change. As a visual aid, I have indicated the 10% error; errors in cosmogenically derived

578   erosion rates are on the order of 10% and given the noise of hilltop curvature (e.g., Hurst

579   *et al.*, 2012; Hurst *et al.*, 2013b) we would likely only be able to estimate D to within 10%

580   even if the landscape was in perfect steady state. It should be noted that the t^* values

581   reported here assume a fixed hillslope length, which might change if only one side of the

582   divide is "pushed" by a pulse of incision (e.g., Mudd and Furbish, 2005). This is why Hurst

583   et al. (2012) focussed on ridgetops with similar slopes on either side of the hilltop.

584

585   Figure 5 shows that under a wide range of background erosion rates and relative changes

586   in the transport coefficient, the time to fall within 10% error usually occurs by $t^* = 0.01$.

587   For $D = 0.001$ m^2 yr^{-1}, $L_H = 25$ m, this means the apparent sediment transport coefficient

588   will be within 10% of the actual value within 625 years, which by geological standards is

589   short. Figure 6 shows the value of the hillslope relaxation time (=~0.4 t^*) as a function of

590   D and L_H. Reported values of D vary over several orders of magnitude but most lie

591   between 0.01 and 0.001 m^2 yr^{-1} (Hurst *et al.*, 2013b). The implication of these results is

592   that in most cases a dramatic change in vegetation would have had to occur within the

593   past few millennia for estimates of D based on CRN derived erosion rates and hilltop

594   curvature to be in error by more than 10%. This is encouraging since the time to reduce

595   the error between apparent and true D is, for most landscapes, shorter than the time

596   elapsed since the younger Dryas period that featured widespread vegetation changes

597   (e.g., Schuman *et al.*, 2002).

598 What effect do varying styles of transience have on the concentration
599 of in-situ cosmogenic nuclides collected in stream sediments?

600 Thus far I have discussed the use of in-situ cosmogenic nuclides such as ^{10}Be and ^{14}C in

601 single regolith profiles but in fact, many, if not most studies that constrain erosion rates,

602 use the technique of detrital CRNs (e.g., Brown *et al.*, 1995; Bierman *et al.*, 1996, Granger

603 *et al.*, 1996). To obtain basin-wide erosion rates, sediment leaving a basin is sampled

604 and the concentration of cosmogenic nuclides in these sediments is used to calculate

605 erosion rates. The technique can even resolve erosion rates if they are spatially

606 heterogeneous (see Granger *et al.*, 1996), but one of the assumptions is that erosion

607 rates should be constant in time in order to estimate the average erosion rate. What if

608 erosion rates are transient? I answer this question using numerical simulations.

609 The model solves a simple governing equation that combines the hillslope flux law of

610 equation (8) with the stream power law that is a simple approximation of channel incision

611 (e.g., Howard, 1994). The resulting conservation equation is:

612

$$\frac{\partial \zeta}{\partial t} = -\nabla \cdot \left[\frac{D \, \nabla \zeta}{1 - \left(\frac{\nabla \zeta}{S_c}\right)^2} \right] - K A^m S^n + U. \tag{13}$$

613

614 where K [L$^{-(2m-1)}$ T^{-1}] is an erodibility coefficient, A [L^2] is the drainage area, S

615 [dimensionless; L/L] is the topographic gradient and U [L T^{-1}] is the tectonic uplift rate. For

616 simplicity, I do not consider density conversion between rock and soil. The FASTSCAPE

617   algorithm of Braun and Willett (2013) is used to solve channel incision, so S is determined

618   along lines of steepest descent to the lowest of the eight neighboring cells (the D8 flow

619   method). For computational efficiency, a D8 scheme is also used to calculate drainage

620   area. Equation (8) is solved with a two dimensional version of the implicit method used in

621   Hurst *et al.* (2013a). The philosophy of this simple approach is that the model should

622   capture the essence of competition between advective (e.g., fluvial) and diffusion like

623   (e.g., hillslope) erosion processes (c.f., Perron *et al.*, 2009).

624

625   The model has its elevation fixed on the north and south boundaries, and the east and

626   west boundaries are periodic. The concentration of ^{10}Be is solved within soil columns

627   throughout the domain using equation (3). This assumes that erosion rates are constant

628   over a model timestep (in the simulations presented here the timestep is 20 years), but

629   erosion rates can change between timesteps. It is assumed that there is no storage of

630   sediment within the channels: once a particle is eroded from the surface of the model it

631   is instantaneously delivered as virtual stream sediment to be queried for the apparent

632   erosion rate using equation (5). The contribution of each column to the collected

633   concentration at the outlet is weighted by each column's erosion rate: this reproduces the

634   weighting in cosmogenic concentrations that are a consequence of greater fluxes

635   originating from portions of the landscape that erode more quickly.

636

637   The model simulations are aimed at probing the effect of changing climatic and base level

638   forcing on apparent erosion rates, similar to studies of Godard *et al*. (2013) and Braun *et*

639   *al*. (2015), but this study differs in its attention to the effect of landscape perturbation on

640   cosmogenic concentrations. Tectonic variations are simulated with time varying uplift. To

641   approximate the effect of a changing climate on the landscape, I vary the fluvial erodibility

642   coefficient, *K*, and the hillslope sediment transport coefficient, *D*. The model was tested

643   with both 40 kyr and 100 kyr cycles. These were to mimic the dominant climate cycles

644   over the past few million years (e.g., Lisiecki and Raymo, 2005). There is no obvious

645   reason to suspect tectonic activity will vary over the same timescale as climate, but uplift

646   is varied over the same period in order to make comparisons between forcings with the

647   same period of variation.

648

649   Two initial landscapes, formed under constant forcing, were used; these were small

650   basins of 5 km^2. The landscapes have an average uplift rate of 0.2 mm yr^{-1}; each

651   simulation begins with a topography adjusted to this erosion rate, with cosmogenic

652   nuclide concentrations set to the steady state concentration (i.e., both the apparent and

653   the actual erosion rates are 0.2 mm yr^{-1} at the beginning of the simulations). All

654   simulations are run with $m = 0.5$, $n = 1$, $S_c = 1$, and all have a mean $D = 0.005$ m^2 yr^{-1}.

655   The first set of simulations have a mean $K = 0.00001$ yr^{-1}. The second set of simulations

656   are run with higher K values (0.00005 yr^{-1}); these are heavily dissected but the high fluvial

657   erodibility coefficient allows tectonic signals to propagate farther into the model domain

658   over an erosion cycle. Relief for the simulations with lower and higher K values begins at

659   ~200 and ~27 meters, respectively (Figure 7).

660

661   The apparent and actual erosion rates for different scenarios are shown in Figure 8. To

662   interpret these plots, it is useful to step back to findings from point models of erosion rates.

663   Several authors have investigated the effect of time varying erosion rates on CRN

664   concentrations (Bierman and Stieg, 1996; Small *et al.*, 1997, Heimsath 2006; Schaller

665   and Ehlers 2006), and their results are useful in understanding CRN concentrations in the

666   context of basin-wide changes in concentrations.

667

668   Schaller and Ehlers (2006) explored periodic forcing of erosion rates and found that the

669   time series of apparent erosion rates was damped compared to the time series of erosion

670   rates. This damping was a function of the mean erosion rate: slower erosion rates

671   featured more damping. In addition, the time series of apparent erosion rates lagged

672   behind that of the actual erosion rates, and the phase shift was a function of the periodicity

673   of the erosion rate variation, with longer period changes in erosion rates resulting in

674   greater phase shift between the apparent and actual erosion rate.

675

676   Another important feature of CRN concentrations in the face of time varying erosion rates

677   was identified by Heimsath (2006): when erosion rates slow significantly, but then speed

678   up once again, there is not enough time to accumulate the nuclides necessary for the

679   apparent erosion rate to reflect the short period of slow erosion rates. This effect can lead

680   to asymmetric damping where the fastest erosion rates are reflected in cosmogenic

681   concentrations but the slowest erosion rates are not (Heimsath, 2006). With these results

682   in mind, we can now examine how apparent erosion rates determined from basin-wide

683 CRNs are affected by variations in forcing factors such as climate and tectonics. I consider

684 only the simplified case of landscapes without significant erosion from mass wasting

685 processes, which can further cloud interpretation of basin averaged CRN concentrations

686 (e.g., Niemi *et al*., 2005; Yanites *et al*., 2009; West *et al*., 2014)

687

Top-down and bottom-up transience

689 Arguably the most striking feature of the time series of apparent erosion rates is the

690 difference between simulations featuring transient uplift rates and those featuring

691 transient K and D (Figures 8 and 9). Panels **a**,**b**, **g** and **j** in Figure 8 depict landscapes in

692 which the uplift rate varies in time, whereas in the other panels uplift is held constant while

693 K and D vary. Where uplift rates vary, the erosion rates and the apparent erosion rates

694 determined from ^{10}Be concentrations are significantly damped relative to changes in uplift

695 rates. Changes in K and D can result in large variations in erosion compared to changes

696 in uplift: in Figure 8 uplift has an amplitude of 100% of the mean uplift, whereas K and D

697 only vary with an amplitude that is 30% of their mean values, yet the variations in erosion

698 rates are much greater for K and D.

699

700 In landscapes with changing erosion rates at base level, signals propagate upstream and

701 upslope (e.g., Whipple and Tucker, 1999). These signals then move up the channel

702 network at a rate controlled by drainage area and the fluvial erodibility coefficient (e.g.,

703 Whipple and Tucker, 1999; Royden and Perron, 2013) and then spread to hillslopes (e.g.,

704 Mudd and Furbish, 2007; Reinhardt *et al*., 2007; Prince and Spotila, 2013). Because

705 these signals propagate upslope, they can be thought of as "bottom-up" drivers of

706 landscape transience (e.g., Bishop, 2007).

707

708 On the other hand, if erodibility coefficients or sediment transport coefficients change, we

709 might reasonably expect the entire landscape to act in concert. For example, both theory

710 (e.g., Whipple and Tucker, 1999) and field studies (e.g., Moon *et al*., 2011; Ferrier *et al*.,

711 2013) suggest that precipitation plays a role in determining the erodibility coefficient (K)

712 of bedrock channels. As a result of climate change, precipitation may change over an

713 entire landscape. Similarly, the hillslope sediment transport coefficient is thought to be a

714 function of landscape properties, such as vegetation cover, that respond to climate (e.g.,

715 Hanks, 2000; Anderson 2002; Dunne *et al*., 2010; Hurst *et al*., 2013b; Pelletier *et al*.,

716 2013; Schlunegger and Norton, 2013; Acosta *et al*., 2015; Andersen et al., 2015). Such

717 changes may be widespread: for example an entire landscape may shift from forest to

718 grassland (e.g., Roering *et al*., 2004; Hughes *et al*., 2009) or diffusive processes may

719 transition from highly efficient frost-related processes to less efficient bioturbation-driven

720 processes (e.g., Hales and Roering, 2009); fluvial processes may then be affected by top

721 down controls on sediment flux (e.g., Wobus et al., 2010). Because such changes act

722 over an entire landscape, these landscapes can be considered to have a "top-down"

723 control on transient erosion. This top down forcing is distributed over the entire catchment,

724 and thus the erosion rate closely follows the changes in sediment transport or erodibility

725 coefficients, mirroring the results presented by Braun *et al.* (2015).

726

Bottom up forcing

Consider the bottom-up scenario (that with varying uplift, U). If uplift forcing is periodic, one finds some parts of the landscape responding to rapid erosion forcing and others responding to slow erosion forcing (Figure 9a-d). For example, in Figure 9b, a period of rapid uplift introduces a wave of fast erosion (as seen in the red area near the boundaries) that has propagated upslope in Figure 9c. The remnant of a previous cycle of fast erosion in Figure 9c exists along the ridgeline. Because the landscape contains both rapidly eroding and slowly eroding areas the erosion rate averaged over the entire landscape is averaged to a value that is very close to the mean uplift rate (Figure 8**a**,**d**,**g**, and **j**). This averaging is reflected in the apparent erosion rates calculated from basin averaged CRN concentrations. It is important to note that this spatial averaging is reliant on the fact that uplift is periodic: rapid erosion rates from one cycle are counterbalanced by slow erosion rates from another. This is not the case if there is a step change or monotonic change in the rate of base level fall (e.g., Rheinhardt et al., 2007; Willenbring et al., 2014).

Top down forcing

Now consider landscapes with top down control on varying erosion. The simulations are set so that the amplitude is 30 % of the mean value, so for example if the mean value of D is 0.005 m^2 yr^{-1}, then D varies between 0.0035 and 0.0065 m^2 yr^{-1}.In these landscapes there still is some spatial variation in erosion rates but the dominant behavior is that when transport coefficients are at their maximum values the erosion rate across the landscape is higher than the time-averaged mean erosion rate (Figure 9f), and conversely low values of the K and D coefficients lead to low erosion rates across the landscape (Figure 9h).

750

751   Between peaks or and troughs in K and D, one can see spatial variations in the erosion

752   rate (Figures 9e, g). This is because these landscapes are more sensitive to changes in

753   D than K (compare, for example, Figure 8b and c, where only small variability in erosion

754   rates from variations in K are apparent). Because hillslope adjust rapidly, their slopes

755   adjacent to channels adjust more quickly to changing D, but the channels must

756   accommodate these changing side slopes (e.g., in Equation 13 the erosion rate in the

757   channel depends on all adjacent pixels). At positions in the landscape with large drainage

758   areas, hillslopes have almost no role because erosion is controlled by channel incision.

759   In contrast, near the tips of the drainage network the effect of side slopes is more

760   substantial since the drainage area along the channel is low and hillslope sediment fluxes

761   are of a similar magnitude to removal of mass by the channel. This could potentially be

762   an artefact of the relative values of K and D in the simulations; higher values of K would

763   reduce this effect. However preliminary simulations featuring K values high enough for

764   channels and hillslopes to respond on similar timescales resulted in unrealistic drainage

765   densities. Landscape dissection is a function of the relative magnitude of K and D (Tucker

766   and Bras, 1998; Perron et al., 2009) and to arrive at landscapes with qualitatively

767   reasonable hillslope lengths (i.e. on the order of tens of meters) I was unable to generate

768   landscapes with channels that responded faster than hillslopes. Relatively fast hillslope

769   response has been documented in natural landscapes (Reinhardt *et al*., 2007; Hurst *et*

770   *al*., 2012) but an exhaustive exploration of K and D to see if this is an expected feature of

771   landscapes is beyond the scope of this study.

772

773 Because erosion rates respond to changing K and D values across the landscape, the

774 erosion rate and the concentration of basin averaged CRNs reflects closely the variation

775 in these parameters (Figures 8b, e, h and k). As predicted in one dimensional simulations,

776 there is greater lag between the basin averaged erosion rate and the apparent erosion

777 rate calculated from CRN concentrations in landscape forced with higher frequency

778 oscillations (compare figures 8b and e).

779

780 In summary, bottom up changes tend to lead to strong spatial variations in erosion rates,

781 but the average erosion rates from basins affected by bottom up forcing remain relatively

782 constant. This is reflected in CRN concentrations. On the other hand, top down forcing

783 results in a more spatially heterogeneous erosion pattern that features strong temporal

784 variation.

785 ## Basin-scale topographic indicators of transience

786 Having examined techniques for determining landscape transience on a hillslope scale,

787 following on from CRN tracing of landscape transience, I now briefly discuss basin and

788 regional scale tracing of landscape transience. Perhaps the most widespread method for

789 looking for differing erosion rates of wide areas is to quantify how steep channels are.

790 Over a century ago, G.K. Gilbert (1877) recognized that topographic gradients drive

791 erosion; in his seminal 1877 report on the geology of the Henry Mountains, he said "we

792 have already seen that erosion is favoured by declivity. If declivity is great the agents of

793 erosion are powerful; where it is small they are weak; where there is no declivity they are

794 powerless." Topographic gradient is still considered one of the driving factors of erosion

795   in channels, along with substrate composition, sediment supply and discharge. The latter

796   varies systematically with drainage area so even if substrate and sediment supply are

797   equal the channel gradient must be normalized for discharge if one is to compare the

798   erosive potential of one channel to another.

799

800   It has been suggested that in eroding landscapes featuring bedrock rivers, channel

801   erosion can be described by the stream power law $E = KA^m S^n$ (e.g., Howard and Kerby,

802   1983; Whipple and Tucker 1999). The equation can be rearranged as $S = (E/K)^{1/n} A^{-m/n}$.

803   The term $(E/K)^{1/n}$ is frequently recast as the steepness index, k_s (which is equal to $SA^{m/n}$

804   according to the equation), or the normalised steepness index k_{sn} if the ratio m/n is set

805   to a fixed reference value (Wobus *et al.*, 2006). The steepness index can be calculated

806   by plotting the logarithm of drainage area against the logarithm of slope (both of these

807   quantities are easily extracted from digital elevation models): if slope-area data is plotted

808   in log-log space, the gradient of a regression line will be $-m/n$ and the intercept where

809    $\log(A) = 0$ will be k_s . Normalized steepness index can be calculated numerically as $k_{sn} =$

810    $SA^{m/n}$ for a fixed value of m/n, frequently set to 0.45 (Wobus *et al.*, 2006). Even if the

811   stream power law is an imperfect description of channel incision (c.f., Lague, 2014), one

812   can still calculate k_{sn} to compare the relative steepness of channels from a purely

813   geometric perspective. The channel steepness index has been used widely to detect

814   regions of anomalously steep channels; these channels can indicate, for example, areas

815   with relatively high tectonic uplift rates (for reviews, see Wobus *et al.*, 2006 and Kirby and

816   Whipple, 2012).

817

818 Another method to investigate the relative steepness of a channel is to use the channel

819 elevations themselves, rescaled either by integrating drainage area as a function of flow

820 distance (e.g., Royden *et al.*, 2000; Perron and Royden, 2013), or by rescaling flow

821 distance by the *m/n* ratio (e.g., Smith *et al.*, 2000; Pritchard *et al.*, 2009). A number of

822 authors have used transformed river profiles to calculate erosion histories using inverse

823 modelling (e.g., Roberts and White, 2010; Fox *et al.*, 2014; Goren *et al.*, 2014; Fox *et al.*,

824 2015; Glotzbach, 2015; Rudge *et al.*, 2015), and these authors have provided valuable

825 constraints on the transient uplift histories of Southern Africa, Australia, Taiwan, the

826 Andes and individual mountain ranges in California.

827

828 One potential pitfall of inversion studies is that if the slope exponent, *n*, does not equal

829 unity, then dynamic information about changing uplift or erosion rates are not entirely

830 preserved by channels (Royden and Perron, 2013). Royden and Perron (2013)

831 demonstrated that for $n > 1$, channel segments generated by periods of faster uplift will

832 consume those generated by slower uplift, whereas for $n < 1$ channel segments

833 generated by slow uplift will consume those generated by rapid uplift; in both cases

834 information about the past is lost. There is evidence that the slope exponent, however, is

835 often not unity (e.g., Snyder *et al.*, 2003; Ouimet *et al.*, 2009; DiBiase *et al.*, 2010;

836 Whittaker and Boulton 2012; Lague 2013; Croissant and Braun, 2014). Even if information

837 is lost, however, one may use statistical methods to look for channel reaches with varying

838   channel steepness, in order to identify reaches that may be eroding at different rates to

839   their neighbors without assuming a historical forcing (e.g., Mudd *et al.*, 2014).

840

841   Another method of looking for landscape transience is to compare a flow length

842   coordinate, normalized for drainage area, across drainage divides. Royden *et al.* (2000)

843   suggested a coordinate transformation:

844

$$\chi = \int_{x_b}^{x} \left(\frac{A_0}{A(x)}\right)^{m/n} dx, \qquad (14)$$

845

846   where A_0 [L^2] is a reference drainage area, introduced to ensure the integrand in equation

847   (14) is dimensionless, x [L] is the distance along the channel and x_b [L] is the location of

848   local base level. The transformed coordinate, χ, has dimensions of length. If channel

849   erosion can be described by the stream power law, then channel elevation can be related

850   to χ with (Perron and Royden, 2013; Royden and Perron, 2013):

851

$$\zeta(x) = \zeta(x_b) + \left(\frac{E}{K A_0^{m}}\right)^{1/n} \chi, \qquad (15)$$

852   Here the gradient of the χ profile, M_χ, that is the channel profile cast as elevation, ζ, plotted

853   as a function of χ, will be indicative of the erosion (or uplift rate if balanced by erosion,

854   i.e., tectonic steady state):

855

$$M_\chi = \left(\frac{E}{K A_0{}^m} \right)^{1/n}, \qquad\qquad (16)$$

856

857   where the chi gradient, M_χ, is related to the channel steepness index by $M_\chi = A_0{}^{-m/n} k_s$.

858

859   Based on equation (15), Willett *et al.* (2014) reasoned that χ is therefore a metric for the

860   steady state elevation of a channel, and therefore in a steady state landscape χ must be

861   balanced across divides. If it is not, then the side of the divide with lower χ will push the

862   divide until equilibrium is restored, a process equivalent to the pushing of divides away

863   from more rapidly eroding channels described by Mudd and Furbish (2005). Figure 10

864   shows an example of the chi coordinate across divides near Sorbas, Spain, the site of a

865   well-documented river capture (e.g., Harvey and Wells, 1987; Stokes *et al.*, 2003). Willett

866   *et al.* (2014) and Yang *et al.* (2015) have used this method to identify potentially

867   widespread areas of stream piracy and drainage reorganisation in the Appalachians of

868   the United States and the Three Rivers region of China. Due to the ease of calculating χ

869   from topographic data, this method promises to help identify regions of transient

870   landscape evolution, as long as author are careful to account for changes in discharge

871   and bedrock erodibility that may complicate comparisons of the χ across adjacent basins.

872

Conclusions: strategies for detecting landscape transience in eroding landscapes

875   In upland, eroding landscapes, detection of transience can be challenging because there

876   are limited depositional archives from which to infer past changes in erosion rates (c.f.,

877   Whittaker *et al*., 2010). However, with judicious use of both topographic and isotopic

878   information, we can gain insight into a landscape's past. Cosmogenic nuclides are a

879   powerful tool for quantifying erosion rates and soil production from the scale of individual

880   soil profiles to entire basins, yet they have been less frequently used to test hypotheses

881   about the past evolution of land surfaces. I have demonstrated that it is possible to use

882   paired cosmogenic nuclides to detect changes in past erosion rates resulting from block

883   removal or acceleration of erosion rates. However, the two nuclides used in the pair must

884   have significantly different decay rates; the only practical way to detect changing erosion

885   rates is by combining the relatively short half-life of cosmogenic in-situ ^{14}C with a longer

886   lived nuclide such as ^{10}Be. Changes in erosion rates or removal of mass is unlikely to be

887   detected if background erosion rates are faster than ~0.1 mm yr^{-1}. When background

888   erosion rates are slower, however, detection is possible. If background erosion rates are

889   ~0.01 mm yr^{-1}, block removal can be detected for up to ~10 kyr after the event.

890   Accelerations in erosion rate can be detected between ~500 years up to ~50 kyr after the

891 event. Decelerations can be detected after ~2 kyr up to, in extreme cases, 500 kyr after

892 the event.

893

894 When we move to the basin or landscape scale, it becomes extremely difficult, if not

895 impossible, to detect landscape transience from basin-wide CRN concentration

896 measurements, and the interpretation of these concentrations is fraught with danger

897 because the response of apparent erosion rates, determined by inverting CRN

898 concentrations, exhibits markedly different behavior depending on how landscape

899 transience is forced. If oscillating landscape transience is forced by changing base level

900 (e.g., through changing sea level or tectonic uplift where differential motion occurs along

901 a fault), then apparent erosion rates will reflect a mean erosion rate averaged over several

902 uplift cycles rather than the current uplift rate. These apparent erosion rates will reflect

903 the actual, basin averaged, erosion rates, but will bear little resemblance to local erosion

904 rates. On the other hand, if erosion rates are transiently forced by climate that affects

905 either channel erodibility or the hillslope sediment transport coefficient, then apparent

906 erosion rates will track the forcing closely over the entire basin. Thus if one is to identify

907 whether apparent erosion rates reflect recent erosion rates or a long term mean, and are

908 consistent with local erosion rates, one must have some constraint on the nature of the

909 transient forcing.

910

911 Topography can complement, or be used in lieu of, CRN data to detect landscape

912 transience. In soil mantled landscapes, the relationship between ridgetop curvature and

913 hillslope relief can be a powerful indicator of landscape transience. Roering *et al.* (2007)

914 demonstrated that normalized forms of relief ($R*$) and hilltop curvature ($E*$) should lie on

915 a single curve if a hillslope is in steady state. Deviations from this curve, therefore, should

916 indicate landscape transience, as demonstrated by Hurst *et al.* (2013a). In this

917 contribution I show that one should be able to resolve a doubling of erosion rate using

918 this technique, and that the signal should persist for hundreds to thousands of years in

919 most landscapes.

920

921 Moving to the scale of basins, both channel steepness, as measured by the normalised

922 steepness index, k_{sn}, or the chi gradient, M_χ, can be indicative of changing erosion rates

923 and landscape transience where other factors, such as sediment supply, or channel

924 substrate, do not vary substantially. The chi coordinate, a coordinate derived by

925 integrating drainage area over channel length, can also be used to identify landscape

926 disequilibrium by looking for variation across drainage divides. Thanks to both

927 geochronologic and topographic tools, geomorphologists now have a variety of tools for

928 examining landscape disequilibrium at scales ranging from single points on the landscape

929 to entire basins. These tools may be used to reconstruct past erosion rates occurring

930 over hundreds to hundreds of thousands of years.

931

Acknowledgements

Software and Data Availability

Scripts for plotting the figures and the source code and data for model simulations are available through github. Figures 1, 2, 8 and 9 are plotted with scripts from https://github.com/simon-m-mudd/CRN_model_plotting. For Figures 3-6 see https://github.com/simon-m-mudd/OneD_hillslope. Figure 7 is plotted using scripts from https://github.com/simon-m-mudd/LSDMappingTools. Figure 10 is generated using code available at https://github.com/LSDtopotools/LSDTopoTools_AnalysisDriver.

References

van Andel TH, Zangger E, Demitrack A. 1990. Land Use and Soil Erosion in Prehistoric and Historical Greece. *Journal of Field Archaeology* **17**: 379–396. DOI: 10.1179/009346990791548628.

Andersen JL, Egholm DL, Knudsen MF, Jansen JD, Nielsen SB. 2015. The periglacial engine of mountain erosion - Part 1: Rates of frost cracking and frost creep. *Earth Surface Dynamics Discussions* **3**: 285–326. DOI: 10.5194/esurfd-3-285-2015.

Anderson RS. 2002. Modeling the tor-dotted crests, bedrock edges, and parabolic profiles of high alpine surfaces of the Wind River Range, Wyoming. *Geomorphology* **46**: 35–58. DOI: 10.1016/S0169-555X(02)00053-3.

Anderson SP, Anderson RS, Tucker GE. 2012. Landscape scale linkages in critical zone evolution. *Comptes Rendus Geoscience* **344**: 586–596. DOI: 10.1016/j.crte.2012.10.008.

Andrews DJ, Bucknam RC. 1987. Fitting degradation of shoreline scarps by a nonlinear diffusion model. *Journal of Geophysical Research: Solid Earth* **92**: 12857–12867. DOI: 10.1029/JB092iB12p12857.

Armitage JJ, Duller RA, Whittaker AC, Allen PA. 2011. Transformation of tectonic and climatic signals from source to sedimentary archive. *Nature Geosci* **4:** 231–235. doi:10.1038/ngeo1087.

Arrowsmith JR, Zielke O. 2009. Tectonic geomorphology of the San Andreas Fault zone from high resolution topography: An example from the Cholame segment. *Geomorphology* **113**: 70–81. DOI: 10.1016/j.geomorph.2009.01.002.

Balco G, Stone JOH. 2005. Measuring middle Pleistocene erosion rates with cosmic-ray-produced nuclides in buried alluvial sediment, Fisher Valley, southeastern Utah. *Earth Surf. Process. Landforms* **30:** 1051–1067. doi:10.1002/esp.1262.

Balco G, Stone JO, Lifton NA, Dunai TJ, 2008. A complete and easily accessible means of calculating surface exposure ages or erosion rates from 10Be and 26Al measurements. *Quaternary Geochronology*, **3:** 174–195. doi:10.1016/j.quageo.2007.12.001.

Bierman PR. 1994. Using in situ produced cosmogenic isotopes to estimate rates of landscape evolution: A review from the geomorphic perspective. *Journal of Geophysical Research: Solid Earth* **99**: 13885–13896. DOI: 10.1029/94JB00459.

Bierman P, Steig EJ. 1996. Estimating Rates of Denudation Using Cosmogenic Isotope Abundances in Sediment. *Earth Surface Processes and Landforms* **21**: 125–139. DOI: 10.1002/(SICI)1096-9837(199602)21:2<125::AID-ESP511>3.0.CO;2-8.

Binnie SA, Phillips WM, Summerfield MA, Fifield LK. 2007. Tectonic uplift, threshold hillslopes, and denudation rates in a developing mountain range. *Geology* **35**: 743–746. DOI: 10.1130/G23641A.1.

Bishop P. 1995. Drainage rearrangement by river capture, beheading and diversion. *Progress in Physical Geography* **19**: 449–473. DOI: 10.1177/030913339501900402.

Bishop P. 2007. Long-term landscape evolution: linking tectonics and surface processes. *Earth Surface Processes and Landforms* **32**: 329–365. DOI: 10.1002/esp.1493.

Bonnet S. 2009. Shrinking and splitting of drainage basins in orogenic landscapes from the migration of the main drainage divide. *Nature Geoscience* **2**: 766–771. DOI: 10.1038/ngeo666.

Braucher R et al. 2013. Determination of muon attenuation lengths in depth profiles from in situ produced cosmogenic nuclides. *Nuclear Instruments and Methods in Physics Research Section B: Beam Interactions with Materials and Atoms* **294**: 484–490. DOI: 10.1016/j.nimb.2012.05.023.

Braun J. 2010. The many surface expressions of mantle dynamics. *Nature Geoscience* **3**: 825–833. DOI: 10.1038/ngeo1020.

Braun J, Simon-Labric T, Murray KE, Reiners PW. 2014. Topographic relief driven by variations in surface rock density. *Nature Geosci* **7:** 534–540. doi:10.1038/ngeo2171.

Braun J, Voisin C, Gourlan AT, Chauvel C. 2015. Erosional response of an actively uplifting mountain belt to cyclic rainfall variations. *Earth Surface Dynamics* **3**: 1–14. DOI: 10.5194/esurf-3-1-2015.

Braun J, Willett SD. 2013. A very efficient O(n), implicit and parallel method to solve the stream power equation governing fluvial incision and landscape evolution. *Geomorphology* **180**: 170–179. DOI: 10.1016/j.geomorph.2012.10.008.

Brown ET, Stallard RF, Larsen MC, Raisbeck GM, Yiou F. 1995. Denudation rates determined from the accumulation of in situ-produced 10Be in the luquillo experimental forest, Puerto Rico. *Earth and Planetary Science Letters* **129**: 193–202. DOI: 10.1016/0012-821X(94)00249-X.

Carslaw HS, Jaeger JC. 1959. *Conduction of heat in solids.* Oxford University Press: Oxford.

Castelltort S, Goren L, Willett SD, Champagnac J-D, Herman F, Braun J. 2012. River drainage patterns in the New Zealand Alps primarily controlled by plate tectonic strain. *Nature Geoscience* **5**: 744–748. DOI: 10.1038/ngeo1582.

Charreau J, Blard P-H, Puchol N, Avouac J-P, Lallier-Vergès E, Bourlès D, Braucher R, Gallaud A, Finkel R, Jolivet M, Chen Y, Roy P. 2011. Paleo-erosion rates in Central Asia since 9 Ma: A transient increase at the onset of Quaternary glaciations? *Earth and Planetary Science Letters* **304:** 85–92. doi:10.1016/j.epsl.2011.01.018.

Chmeleff J, von Blanckenburg F, Kossert K, Jakob D. 2010. Determination of the 10Be half-life by multicollector ICP-MS and liquid scintillation counting. *Nuclear Instruments and Methods in Physics Research Section B: Beam Interactions with Materials and Atoms* **268:** 192–199. doi:10.1016/j.nimb.2009.09.012.

Clubb FJ, Mudd SM, Milodowski DT, Hurst MD, Slater LJ. 2014. Objective extraction of channel heads from high-resolution topographic data. *Water Resources Research* **50**: 4283–4304. DOI: 10.1002/2013WR015167.

Coulthard TJ, Van de Wiel MJ. 2013. Climate, tectonics or morphology: what signals can we see in drainage basin sediment yields? *Earth Surface Dynamics* **1**: 13–27. DOI: 10.5194/esurf-1-13-2013.

1027 Croissant T, Braun J. 2014. Constraining the stream power law: a novel approach
1028 combining a landscape evolution model and an inversion method. *Earth Surface*
1029 *Dynamics* **2**: 155–166. DOI: 10.5194/esurf-2-155-2014.

1030 Culling WEH. 1960. Analytical Theory of Erosion. *The Journal of Geology* **68**: 336–344.

1031 Davis WM. 1889. *The Rivers and Valleys of Pennsylvania*. National Geographic Society:
1032 Washington.

1033 Davis WM. 1899. The Geographical Cycle. *The Geographical Journal* **14**: 481–504. DOI:
1034 10.2307/1774538.

1035 DiBiase RA, Heimsath AM, Whipple KX. 2012. Hillslope response to tectonic forcing in
1036 threshold landscapes. *Earth Surface Processes and Landforms* **37**: 855–865. DOI:
1037 10.1002/esp.3205.

1038 DiBiase RA, Whipple KX, Heimsath AM, Ouimet WB. 2010. Landscape form and
1039 millennial erosion rates in the San Gabriel Mountains, CA. *Earth and Planetary Science*
1040 *Letters* **289**: 134–144. DOI: 10.1016/j.epsl.2009.10.036.

1041 Dietrich WE, Bellugi DG, Sklar LS, Stock JD, Heimsath AM, Roering JJ. 2003.
1042 Geomorphic Transport Laws for Predicting Landscape form and Dynamics. In *Prediction*
1043 *in Geomorphology* , Wilcock PR and Iverson RM (eds). American Geophysical Union;
1044 103–132.

1045 Dubayah RO, Drake JB. 2000. Lidar Remote Sensing for Forestry. *Journal of Forestry*
1046 **98**: 44–46.

1047 Dunai TJ. 2010. *Cosmogenic Nuclides: Principles, Concepts and Applications in the Earth*
1048 *Surface Sciences.* Cambridge University Press: Cambridge.

1049 Dunne T, Malmon DV, Mudd SM. 2010. A rain splash transport equation assimilating field
1050 and laboratory measurements. *Journal of Geophysical Research-Earth Surface* **115**:
1051 F01001. DOI: 10.1029/2009JF001302.

1052 Ferrier KL, Huppert KL, Perron JT. 2013. Climatic control of bedrock river incision. *Nature*
1053 **496**: 206–209. DOI: 10.1038/nature11982.

1054 Fox M, Goren L, May DA, Willett SD. 2014. Inversion of fluvial channels for paleorock
1055 uplift rates in Taiwan. *Journal of Geophysical Research: Earth Surface* **119**: 1853–1875.
1056 DOI: 10.1002/2014JF003196.

1057 Fulop RH, Naysmith P, Cook GT, Fabel D, Xu S, Bishop P. 2010. Update on the
1058 Performance of the SUERC In Situ Cosmogenic 14C Extraction Line. *Radiocarbon* **52**:
1059 1288–1294. DOI: 10.2458/azu_js_rc.52.3627.

1060 Gabet EJ, Perron JT, Johnson DL. 2014. Biotic origin for Mima mounds supported by
1061 numerical modeling. *Geomorphology* **206**: 58–66. DOI:
1062 10.1016/j.geomorph.2013.09.018.

1063 Gabet EJ, Mudd SM, Milodowski DT, Yoo K, Hurst MD, Dosseto A. 2015. Local
1064 topography and erosion rate control regolith thickness along a ridgeline in the Sierra
1065 Nevada, California. *Earth Surface Processes and Landforms* **40:** 1779-1790. DOI:
1066 10.1002/esp.3754.

1067 Gallen SF, Wegmann KW, Frankel KL, Hughes S, Lewis RQ, Lyons N, Paris P, Ross K,
1068 Bauer JB, Witt AC. 2011. Hillslope response to knickpoint migration in the Southern
1069 Appalachians: implications for the evolution of post-orogenic landscapes. *Earth Surface*
1070 *Processes and Landforms* **36**: 1254–1267. DOI: 10.1002/esp.2150.

1071 Gilbert GK. 1877. *Geology of the Henry Mountains.* USGS Unnumbered Series.
1072 Government Printing Office: Washington, D.C.

1073 Gilbert GK. 1909. The Convexity of Hilltops. *Journal of Geology* **17**: 344–350. DOI:
1074 10.1086/621620.

1075 Glotzbach C. 2015. Deriving rock uplift histories from data-driven inversion of river
1076 profiles. *Geology* **43**: 467–470. DOI: 10.1130/G36702.1.

1077 Godard V, Tucker GE, Burch Fisher G, Burbank DW, Bookhagen B. 2013. Frequency-
1078 dependent landscape response to climatic forcing. *Geophysical Research Letters* **40**:
1079 859–863. DOI: 10.1002/grl.50253.

1080 Goehring BM, Schimmelpfennig I, Schaefer JM. 2014. Capabilities of the Lamont–
1081 Doherty Earth Observatory in situ 14C extraction laboratory updated. *Quaternary*
1082 *Geochronology* **19**: 194–197. DOI: 10.1016/j.quageo.2013.01.004.

1083 Goren L, Fox M, Willett SD. 2014a. Tectonics from fluvial topography using formal linear
1084 inversion: Theory and applications to the Inyo Mountains, California. *Journal of*
1085 *Geophysical Research: Earth Surface* **119**: 1651–1681. DOI: 10.1002/2014JF003079.

1086 Goren L, Willett SD, Herman F, Braun J. 2014b. Coupled numerical-analytical approach
1087 to landscape evolution modeling. *Earth Surface Processes and Landforms* **39**: 522–545.
1088 DOI: 10.1002/esp.3514.

1089 Granger DE. 2006. A review of burial dating methods using 26Al and 10Be. *Geological*
1090 *Society of America Special Papers* **415**: 1–16. DOI: 10.1130/2006.2415(01).

1091 Granger DE, Kirchner JW, Finkel R. 1996. Spatially Averaged Long-Term Erosion Rates
1092 Measured from in Situ-Produced Cosmogenic Nuclides in Alluvial Sediment. *The Journal*
1093 *of Geology* **104**: 249–257.

1094 Granger DE, Lifton NA, Willenbring JK. 2013. A cosmic trip: 25 years of cosmogenic
1095 nuclides in geology. *Geological Society of America Bulletin* **125**: 1379–1402. DOI:
1096 10.1130/B30774.1.

1097 Granger DE, Smith AL. 2000. Dating buried sediments using radioactive decay and
1098 muogenic production of 26Al and 10Be. *Nuclear Instruments and Methods in Physics*
1099 *Research Section B: Beam Interactions with Materials and Atoms* **172**: 822–826. DOI:
1100 10.1016/S0168-583X(00)00087-2.

1101 Grieve SWD, Mudd SM, Hurst MD. 2016. How long is a hillslope? *Earth Surf. Process.*
1102 *Landforms* doi:10.1002/esp.3884.

1103 Hales TC, Roering JJ. 2009. A frost "buzzsaw" mechanism for erosion of the eastern
1104 Southern Alps, New Zealand. *Geomorphology* **107**: 241–253. DOI:
1105 10.1016/j.geomorph.2008.12.012.

1106 Hanks TC. 2000. The age of scarplike landforms from diffusion-equation analysis. In
1107 *Quaternary Geochronology: Methods and Applications, edited by J. Stratton Noller, J. M.*
1108 *Sowers, and W. R. Lettis.* American Geophysical Union: Washington, D.C.; 313–338.

1109 Hartley RA, Roberts GG, White N, Richardson C. 2011. Transient convective uplift of an
1110 ancient buried landscape. *Nature Geoscience* **4**: 562–565. DOI: 10.1038/ngeo1191.

1111 Harvey AM, Wells SG. 1987. Response of Quaternary fluvial systems to differential
1112 epeirogenic uplift: Aguas and Feos river systems, southeast Spain. *Geology* **15**: 689–
1113 693. DOI: 10.1130/0091-7613(1987)15<689:ROQFST>2.0.CO;2.

1114 Hasbargen LE, Paola C. 2000. Landscape instability in an experimental drainage basin.
1115 *Geology* **28**: 1067–1070. DOI: 10.1130/0091-7613(2000)28<1067:LIIAED>2.0.CO;2.

1116 Heimsath AM. 2006. Eroding the land: Steady-state and stochastic rates and processes
1117 through a cosmogenic lens. *Geological Society of America Special Papers* **415**: 111–129.
1118 DOI: 10.1130/2006.2415(07).

1119 Heimsath AM, E. Dietrich W, Nishiizumi K, Finkel RC. 1999. Cosmogenic nuclides,
1120 topography, and the spatial variation of soil depth. *Geomorphology* **27**: 151–172. DOI:
1121 10.1016/S0169-555X(98)00095-6.

1122 Heimsath AM, Furbish DJ, Dietrich WE. 2005. The illusion of diffusion: Field evidence for
1123 depth-dependent sediment transport. *Geology* **33**: 949–952. DOI: 10.1130/G21868.1.

1124 Heisinger B, Lal D, Jull AJT, Kubik P, Ivy-Ochs S, Knie K, Nolte E. 2002a. Production of
1125 selected cosmogenic radionuclides by muons: 2. Capture of negative muons. *Earth and*
1126 *Planetary Science Letters* **200**: 357–369. DOI: 10.1016/S0012-821X(02)00641-6.

1127 Heisinger B, Lal D, Jull AJT, Kubik P, Ivy-Ochs S, Neumaier S, Knie K, Lazarev V, Nolte
1128 E. 2002b. Production of selected cosmogenic radionuclides by muons: 1. Fast muons.
1129 *Earth and Planetary Science Letters* **200**: 345–355. DOI: 10.1016/S0012-
1130 821X(02)00640-4.

1131 Hippe K, Kober F, Wacker L, Fahrni SM, Ivy-Ochs S, Akçar N, Schlüchter C, Wieler R.
1132 2013. An update on in situ cosmogenic 14C analysis at ETH Zürich. *Nuclear Instruments*
1133 *and Methods in Physics Research Section B: Beam Interactions with Materials and Atoms*
1134 **294**: 81–86. DOI: 10.1016/j.nimb.2012.06.020.

1135 Howard A. 1994. A Detachment-Limited Model of Drainage-Basin Evolution. *Water*
1136 *Resources Research* **30**: 2261–2285. DOI: 10.1029/94WR00757.

1137 Hughes MW, Almond PC, Roering JJ. 2009. Increased sediment transport via
1138 bioturbation at the last glacial-interglacial transition. *Geology* **37**: 919–922. DOI:
1139 10.1130/G30159A.1.

1140 Hurst MD, Mudd SM, Attal M, Hilley G. 2013a. Hillslopes Record the Growth and Decay
1141 of Landscapes. *Science* **341**: 868–871. DOI: 10.1126/science.1241791.

1142 Hurst MD, Mudd SM, Walcott R, Attal M, Yoo K. 2012. Using hilltop curvature to derive
1143 the spatial distribution of erosion rates. *Journal of Geophysical Research: Earth Surface*
1144 **117**: F02017. DOI: 10.1029/2011JF002057.

1145 Hurst MD, Mudd SM, Yoo K, Attal M, Walcott R. 2013b. Influence of lithology on hillslope
1146 morphology and response to tectonic forcing in the northern Sierra Nevada of California.
1147 *Journal of Geophysical Research-Earth Surface* **118**: 832–851. DOI: 10.1002/jgrf.20049.

1148 Jerolmack DJ, Paola C. 2010. Shredding of environmental signals by sediment transport.
1149 *Geophysical Research Letters* **37**: L19401. DOI: 10.1029/2010GL044638.

1150 Judson S. 1968. Erosion of the Land, or what's happening to our continents? *American
1151 Scientist* **56**: 356–374.

1152 Jungers MC, Bierman PR, Matmon A, Nichols K, Larsen J, Finkel R. 2009. Tracing
1153 hillslope sediment production and transport with in situ and meteoric 10Be. *Journal of
1154 Geophysical Research: Earth Surface* **114**: F04020. DOI: 10.1029/2008JF001086.

1155 Kirby E, Whipple KX. 2012. Expression of active tectonics in erosional landscapes.
1156 *Journal of Structural Geology* **44**: 54–75. DOI: 10.1016/j.jsg.2012.07.009.

1157 Korschinek G, Bergmaier A, Faestermann T, Gerstmann UC, Knie K, Rugel G, Wallner
1158 A, Dillmann I, Dollinger G, von Gostomski CL, Kossert K, Maiti M, Poutivtsev M, Remmert,
1159 A, 2010. A new value for the half-life of 10Be by Heavy-Ion Elastic Recoil Detection and
1160 liquid scintillation counting. *Nuclear Instruments and Methods in Physics Research
1161 Section B: Beam Interactions with Materials and Atoms* **268:** 187–191.
1162 doi:10.1016/j.nimb.2009.09.020.

1163 Lague D. 2014. The stream power river incision model: evidence, theory and beyond.
1164 *Earth Surface Processes and Landforms* **39**: 38–61. DOI: 10.1002/esp.3462.

1165 Lague D, Crave A, Davy P. 2003. Laboratory experiments simulating the geomorphic
1166 response to tectonic uplift. *Journal of Geophysical Research: Solid Earth* **108**: 2008. DOI:
1167 10.1029/2002JB001785.

1168 Lal D. 1991. Cosmic ray labeling of erosion surfaces: in situ nuclide production rates and
1169 erosion models. *Earth and Planetary Science Letters* **104**: 424–439. DOI: 10.1016/0012-
1170 821X(91)90220-C.

1171 Lefsky MA, Cohen WB, Parker GG, Harding DJ. 2002. Lidar Remote Sensing for
1172 Ecosystem Studies Lidar, an emerging remote sensing technology that directly measures
1173 the three-dimensional distribution of plant canopies, can accurately estimate vegetation
1174 structural attributes and should be of particular interest to forest, landscape, and global

ecologists. *BioScience* **52**: 19–30. DOI: 10.1641/0006-3568(2002)052[0019:LRSFES]2.0.CO;2.

Lisiecki LE, Raymo ME. 2005. A Pliocene-Pleistocene stack of 57 globally distributed benthic delta O-18 records. *Paleoceanography* **20**: PA1003. DOI: 10.1029/2004PA001071.

Marshall JA, Roering JJ, Bartlein PJ, Gavin DG, Granger DE, Rempel A., Praskievicz, SJ, Hales, TC, 2015. Frost for the trees: Did climate increase erosion in unglaciated landscapes during the late Pleistocene? *Science Advances* **1**. e1500715. doi:10.1126/sciadv.1500715

McKean JA, Dietrich WE, Finkel RC, Southon JR, Caffee MW. 1993. Quantification of soil production and downslope creep rates from cosmogenic 10Be accumulations on a hillslope profile. *Geology* **21**: 343–346. DOI: 10.1130/0091-7613(1993)021<0343:QOSPAD>2.3.CO;2.

Milodowski DT, Mudd SM, Mitchard ETA. 2015. Topographic roughness as a signature of the emergence of bedrock in eroding landscapes. *Earth Surface Dynamics* **3**: 483-499. DOI 10.5194/esurf-3-483-2015.

Molnar P, Tapponnier P. 1975. Cenozoic Tectonics of Asia: Effects of a Continental Collision: Features of recent continental tectonics in Asia can be interpreted as results of the India-Eurasia collision. *Science* **189**: 419–426. DOI: 10.1126/science.189.4201.419.

Moon S, Page Chamberlain C, Blisniuk K, Levine N, Rood DH, Hilley GE. 2011. Climatic control of denudation in the deglaciated landscape of the Washington Cascades. *Nature Geoscience* **4**: 469–473. DOI: 10.1038/ngeo1159.

Moucha R, Forte AM. 2011. Changes in African topography driven by mantle convection. *Nature Geoscience* **4**: 707–712. DOI: 10.1038/ngeo1235.

Mudd SM, Furbish DJ. 2005. Lateral migration of hillcrests in response to channel incision in soil-mantled landscapes. *Journal of Geophysical Research: Earth Surface* **110**: F04026. DOI: 10.1029/2005JF000313.

Mudd SM, Furbish DJ. 2007. Responses of soil-mantled hillslopes to transient channel incision rates. *Journal of Geophysical Research-Earth Surface* **112**: F03S18. DOI: 10.1029/2006JF000516.

Mudd SM, Attal M, Milodowski DT, Grieve SWD, Valters DA. 2014. A statistical framework to quantify spatial variation in channel gradients using the integral method of channel profile analysis. *Journal of Geophysical Research-Earth Surface* **119**: 138–152. DOI: 10.1002/2013JF002981.

Muzikar P. 2009. General models for episodic surface denudation and its measurement by cosmogenic nuclides. *Quaternary Geochronology* **4**: 50–55. DOI: 10.1016/j.quageo.2008.06.004.

Niemi NA, Oskin M, Burbank DW, Heimsath AM, Gabet EJ. 2005. Effects of bedrock landslides on cosmogenically determined erosion rates. *Earth and Planetary Science Letters* **237**: 480–498. DOI: 10.1016/j.epsl.2005.07.009.

Nishiizumi K. 2004. Preparation of 26Al AMS standards. *Nuclear Instruments and Methods in Physics Research Section B: Beam Interactions with Materials and Atoms* **223–224:** 388–392. doi:10.1016/j.nimb.2004.04.075.

Orlandini S, Tarolli P, Moretti G, Dalla Fontana G. 2011. On the prediction of channel heads in a complex alpine terrain using gridded elevation data. *Water Resources Research* **47**: W02538. DOI: 10.1029/2010WR009648.

Ouimet WB, Whipple KX, Granger DE. 2009. Beyond threshold hillslopes: Channel adjustment to base-level fall in tectonically active mountain ranges. *Geology* **37**: 579–582. DOI: 10.1130/G30013A.1.

Parker G, Perg LA. 2005. Probabilistic formulation of conservation of cosmogenic nuclides: effect of surface elevation fluctuations on approach to steady state. *Earth Surface Processes and Landforms* **30**: 1127–1144. DOI: 10.1002/esp.1266.

Passalacqua P, Do Trung T, Foufoula-Georgiou E, Sapiro G, Dietrich WE. 2010. A geometric framework for channel network extraction from lidar: Nonlinear diffusion and geodesic paths. *Journal of Geophysical Research: Earth Surface* **115**: F01002. DOI: 10.1029/2009JF001254.

Passalacqua P et al. 2015. Analyzing high resolution topography for advancing the understanding of mass and energy transfer through landscapes: A review. *Earth-Science Reviews* **148**: 174–193. DOI: 10.1016/j.earscirev.2015.05.012.

Pelletier JD. 2004. Persistent drainage migration in a numerical landscape evolution model. *Geophysical Research Letters* **31**: L20501. DOI: 10.1029/2004GL020802.

Pelletier JD. 2013. A robust, two-parameter method for the extraction of drainage networks from high-resolution digital elevation models (DEMs): Evaluation using synthetic and real-world DEMs. *Water Resources Research* **49**: 75–89. DOI: 10.1029/2012WR012452.

Pelletier JD et al. 2013. Coevolution of nonlinear trends in vegetation, soils, and topography with elevation and slope aspect: A case study in the sky islands of southern Arizona. *Journal of Geophysical Research-Earth Surface* **118**: 741–758. DOI: 10.1002/jgrf.20046.

Perron JT, Kirchner JW, Dietrich WE. 2009. Formation of evenly spaced ridges and valleys. *Nature* **460**: 502–505. DOI: 10.1038/nature08174.

Perron JT, Royden L. 2013. An integral approach to bedrock river profile analysis. *Earth Surface Processes and Landforms* **38**: 570–576. DOI: 10.1002/esp.3302.

Portenga EW, Bierman PR. 2011. Understanding Earth's eroding surface with 10Be. *GSA Today* **21**: 4–10. DOI: 10.1130/G111A.1.

1250 Prince PS, Spotila JA. 2013. Evidence of transient topographic disequilibrium in a
1251 landward passive margin river system: knickpoints and paleo-landscapes of the New
1252 River basin, southern Appalachians. *Earth Surface Processes and Landforms* **38**: 1685–
1253 1699. DOI: 10.1002/esp.3406.

1254 Pritchard D, Roberts GG, White NJ, Richardson CN. 2009. Uplift histories from river
1255 profiles. *Geophysical Research Letters* **36**: L24301. DOI: 10.1029/2009GL040928.

1256 Reinhardt LJ, Bishop P, Hoey TB, Dempster TJ, Sanderson DCW. 2007. Quantification
1257 of the transient response to base-level fall in a small mountain catchment: Sierra Nevada,
1258 southern Spain. *Journal of Geophysical Research: Earth Surface* **112**: F03S05. DOI:
1259 10.1029/2006JF000524.

1260 Riggins SG, Anderson RS, Anderson SP, Tye AM. 2011. Solving a conundrum of a
1261 steady-state hilltop with variable soil depths and production rates, Bodmin Moor, UK.
1262 *Geomorphology* **128**: 73–84. DOI: 10.1016/j.geomorph.2010.12.023.

1263 Roberts GG, White N. 2010. Estimating uplift rate histories from river profiles using
1264 African examples. *Journal of Geophysical Research* **115**: DOI: 10.1029/2009JB006692.

1265 Roering JJ, Kirchner JW, Dietrich WE. 1999. Evidence for nonlinear, diffusive sediment
1266 transport on hillslopes and implications for landscape morphology. *Water Resources
1267 Research* **35**: 853–870. DOI: 10.1029/1998WR900090.

1268 Roering JJ, Kirchner JW, Dietrich WE. 2001. Hillslope evolution by nonlinear, slope-
1269 dependent transport: Steady state morphology and equilibrium adjustment timescales.
1270 *Journal of Geophysical Research: Solid Earth* **106**: 16499–16513. DOI:
1271 10.1029/2001JB000323.

1272 Roering JJ, Almond P, Tonkin P, McKean J. 2004. Constraining climatic controls on
1273 hillslope dynamics using a coupled model for the transport of soil and tracers: Application
1274 to loess-mantled hillslopes, South Island, New Zealand. *Journal of Geophysical
1275 Research-Earth Surface* **109**: F01010. DOI: 10.1029/2003JF000034.

1276 Roering JJ, Perron JT, Kirchner JW. 2007. Functional relationships between denudation
1277 and hillslope form and relief. *Earth and Planetary Science Letters* **264**: 245–258. DOI:
1278 10.1016/j.epsl.2007.09.035.

1279 Roering JJ. 2008. How well can hillslope evolution models "explain" topography?
1280 Simulating soil transport and production with high-resolution topographic data. *Geological
1281 Society of America Bulletin* **120**: 1248–1262. DOI: 10.1130/B26283.1.

1282 Roering JJ, Marshall J, Booth AM, Mort M, Jin Q. 2010. Evidence for biotic controls on
1283 topography and soil production. *Earth and Planetary Science Letters* **298**: 183–190. DOI:
1284 10.1016/j.epsl.2010.07.040.

1285 Rohrman M, van der Beek P. 1996. Cenozoic postrift domal uplift of North Atlantic
1286 margins: An asthenospheric diapirism model. *Geology* **24:** 901–904. doi:10.1130/0091-
1287 7613(1996)024<0901:CPDUON>2.3.CO;2.

1288 Rood DH, Hall S, Guilderson TP, Finkel RC, Brown TA. 2010. Challenges and
1289 opportunities in high-precision Be-10 measurements at CAMS. *Nuclear Instruments and*
1290 *Methods in Physics Research Section B: Beam Interactions with Materials and Atoms*
1291 **268**: 730–732. DOI: 10.1016/j.nimb.2009.10.016.

1292 Royden LH, Clark MK, Whipple KX. 2000. Evolution of river elevation profiles by bedrock
1293 incision: Analytical solutions for transient river profiles related to changing uplift and
1294 precipitation rates. *Eos (Transactions, American Geophysical Union)* **81, Fall Meeting**
1295 **Supplement**: Abstract T62F–09.

1296 Royden L, Perron JT. 2013. Solutions of the stream power equation and application to
1297 the evolution of river longitudinal profiles. *Journal of Geophysical Research: Earth*
1298 *Surface* **118**: 497–518. DOI: 10.1002/jgrf.20031.

1299 Rudge JF, Roberts GG, White NJ, Richardson CN. 2015. Uplift histories of Africa and
1300 Australia from linear inverse modeling of drainage inventories. *Journal of Geophysical*
1301 *Research: Earth Surface* 2014JF003297. DOI: 10.1002/2014JF003297.

1302 Saunders AD, Jones SM, Morgan LA, Pierce KL, Widdowson M, Xu YG. 2007. Regional
1303 uplift associated with continental large igneous provinces: The roles of mantle plumes
1304 and the lithosphere. *Chemical Geology* **241:** 282–318.
1305 doi:10.1016/j.chemgeo.2007.01.017.

1306 Schaller M, von Blanckenburg F, Veldkamp A, Tebbens LA, Hovius N, Kubik PW. 2002.
1307 A 30 000 yr record of erosion rates from cosmogenic 10Be in Middle European river
1308 terraces. *Earth and Planetary Science Letters* **204:** 307–320. doi:10.1016/S0012-
1309 821X(02)00951-2.

1310 Schaller M, Ehlers TA. 2006. Limits to quantifying climate driven changes in denudation
1311 rates with cosmogenic radionuclides. *Earth and Planetary Science Letters* **248**: 153–167.
1312 DOI: 10.1016/j.epsl.2006.05.027.

1313 Schlunegger F, Norton KP. 2013. Water versus ice: The competing roles of modern
1314 climate and Pleistocene glacial erosion in the Central Alps of Switzerland. *Tectonophysics*
1315 **602**: 370–381. DOI: 10.1016/j.tecto.2013.03.027.

1316 Schoenbohm LM, Whipple KX, Burchfiel BC, Chen L. 2004. Geomorphic constraints on
1317 surface uplift, exhumation, and plateau growth in the Red River region, Yunnan Province,
1318 China. *Geological Society of America Bulletin* **116**: 895–909. DOI: 10.1130/B25364.1.

1319 Sherrod BL, Brocher TM, Weaver CS, Bucknam RC, Blakely RJ, Kelsey HM, Nelson AR,
1320 Haugerud R. 2004. Holocene fault scarps near Tacoma, Washington, USA. *Geology* **32**:
1321 9–12. DOI: 10.1130/G19914.1.

1322 Shuman B, Webb T, Bartlein P, Williams JW. 2002. The anatomy of a climatic oscillation:
1323 vegetation change in eastern North America during the Younger Dryas chronozone.
1324 *Quaternary science reviews* **21**: 1777–1791.

Slatton KC, Carter WE, Shrestha RL, Dietrich W. 2007. Airborne Laser Swath Mapping: Achieving the resolution and accuracy required for geosurficial research. *Geophysical Research Letters* **34**: L23S10. DOI: 10.1029/2007GL031939.

Small EE, Anderson RS, Hancock GS. 1999. Estimates of the rate of regolith production using 10Be and 26Al from an alpine hillslope. *Geomorphology* **27**: 131–150. DOI: 10.1016/S0169-555X(98)00094-4.

Smith TR, Merchant GE, Birnir B. 1997. Towards an elementary theory of drainage basin evolution: II. A computational evaluation. *Computers & Geosciences* **23**: 823–849. DOI: 10.1016/S0098-3004(97)00067-8.

Smith TR, Merchant GE, Birnir B. 2000. Transient Attractors: Towards a Theory of the Graded Stream for Alluvial and Bedrock Channels. *Comput. Geosci.* **26**: 541–580. DOI: 10.1016/S0098-3004(99)00128-4.

Snyder NP, Whipple KX, Tucker GE, Merritts DJ. 2003. Importance of a stochastic distribution of floods and erosion thresholds in the bedrock river incision problem. *Journal of Geophysical Research: Solid Earth* **108**: 2117. DOI: 10.1029/2001JB001655.

Stokes M, Mather AE, Harvey AM. 2002. Quantification of river-capture-induced base-level changes and landscape development, Sorbas Basin, SE Spain. *Geological Society, London, Special Publications* **191**: 23–35. DOI: 10.1144/GSL.SP.2002.191.01.03.

Tarolli P. 2014. High-resolution topography for understanding Earth surface processes: Opportunities and challenges. *Geomorphology* **216**: 295–312. DOI: 10.1016/j.geomorph.2014.03.008.

Torres Acosta V, Schildgen TF, Clarke BA, Scherler D, Bookhagen B, Wittmann H, Blanckenburg F von, Strecker MR. 2015. Effect of vegetation cover on millennial-scale landscape denudation rates in East Africa. *Lithosphere* L402.1. DOI: 10.1130/L402.1.

Tucker GE, Bras RL. 1998. Hillslope processes, drainage density, and landscape morphology. *Water Resources Research* **34**: 2751–2764. DOI: 10.1029/98WR01474.

Vermeesch P. 2007. CosmoCalc: An Excel add-in for cosmogenic nuclide calculations. *Geochemistry, Geophysics, Geosystems* **8**: Q08003. DOI: 10.1029/2006GC001530.

West AJ, Hetzel R, Li G, Jin Z, Zhang F, Hilton RG, Densmore AL. 2014. Dilution of 10Be in detrital quartz by earthquake-induced landslides: Implications for determining denudation rates and potential to provide insights into landslide sediment dynamics. *Earth and Planetary Science Letters* **396**: 143–153. DOI: 10.1016/j.epsl.2014.03.058.

Whittaker AC. 2012. How do landscapes record tectonics and climate? *Lithosphere* **4**: 160–164. DOI: 10.1130/RF.L003.1.

Whittaker AC, Attal M, Allen PA. 2010. Characterising the origin, nature and fate of sediment exported from catchments perturbed by active tectonics. *Basin Research* **22**: 809–828. DOI: 10.1111/j.1365-2117.2009.00447.x.

Whittaker AC, Boulton SJ. 2012. Tectonic and climatic controls on knickpoint retreat rates and landscape response times. *Journal of Geophysical Research: Earth Surface* **117**: F02024. DOI: 10.1029/2011JF002157.

Willenbring JK, Gasparini NM, Crosby BT, Brocard G. 2013. What does a mean mean? The temporal evolution of detrital cosmogenic denudation rates in a transient landscape. *Geology* **41:** 1215-1218. G34746.1. doi:10.1130/G34746.1.

Willett SD, McCoy SW, Perron JT, Goren L, Chen C-Y. 2014. Dynamic Reorganization of River Basins. *Science* **343**: 1248765. DOI: 10.1126/science.1248765.

Wobus CW, Tucker GE, Anderson RS. 2010. Does climate change create distinctive patterns of landscape incision? *Journal of Geophysical Research: Earth Surface* **115**: F04008. DOI: 10.1029/2009JF001562.

Yang R, Willett SD, Goren L. 2015. In situ low-relief landscape formation as a result of river network disruption. *Nature* **520**: 526–529. DOI: 10.1038/nature14354.

Yanites BJ, Tucker GE, Anderson RS. 2009. Numerical and analytical models of cosmogenic radionuclide dynamics in landslide-dominated drainage basins. *Journal of Geophysical Research* **114**: DOI: 10.1029/2008JF001088.

Figure Captions

Figure 1. Ratio of the apparent erosion rate calculated from ^{14}C to the apparent erosion rate calculated from ^{10}Be if a block is removed at some time in the past. The depth of block removal (d_{br}) is listed in each panel. The dashed and solid lines in each panel represent different background erosion rates. An erosion rate of 0.0026 g cm^2 yr^{-1} is equivalent to an erosion rate of 0.01 mm yr^{-1} if the rock density is 2.6 g cm^{-3}. The shaded area denotes a 20% difference between erosion rates predicted by in-situ ^{14}C and ^{10}Be; differences below this are likely undetectable.

1388 **Figure 2.** Ratio of the apparent erosion rate calculated from ^{14}C to the apparent erosion

1389 rate calculated from [10]Be if there is a step change in erosion rate at some time in the past.

1390 Panel **a.** shows scenarios in which erosion rates increase, whereas panel **b.** shows

1391 scenarios in which erosion rates decrease. The shaded area denotes a 20% difference

1392 between erosion rates predicted by in-situ ^{14}C and [10]Be; differences below this are likely

1393 undetectable.

1394

1395 **Figure 3.** Responses of hillslopes to transient perturbation. Panel **a.** shows in black the

1396 curve of dimensionless relief vs dimensionless erosion rate predicted by Roering *et al*.,

1397 (2008). The red and green curves show the effect of an increase of erosion rate of two

1398 and one orders of magnitude, respectively; stars represent starting and ending positions

1399 on the steady state curve. Increased erosion rates result in hillslopes that plot above the

1400 steady state curve. Panel **b.** shows a dimensionless hillslope profile. The blue profile is

1401 the initial condition, the green curve shows the profile after a dimensionless time (t^*) of

1402 0.05 (that is, after 0.05 times L_H^2/D) following an order of magnitude increase in erosion

1403 rate. The dashed grey curve shows a steady state hillslope with the same ridgetop

1404 curvature as the green profile, demonstrating that the steady profile has lower relief than

1405 the transient profile and illustrating why hillslopes that have increased erosion rates plot

1406 above the steady profile in dimensionless relief vs. apparent erosion rate plots.

1407

1408 **Figure 4.** Detection and duration of transience in hillslope profiles in the case of a step

1409 change in erosion rate. Panel **a.** shows maximum differences between predicted and

1410   measured dimensionless relief (R^*) as a function of both initial erosion rate and the ratio

1411   between initial and final erosion rates. Perturbations within the shaded area are unlikely

1412   to be detected using E^* vs R^*. The size of the shaded region will depend on the landscape

1413   and is determined by the standard error in R^*. Panel **b.** shows the time to the maximum

1414   difference in R^*; steeper landscapes (higher E^*) have shorter response times because

1415   more of the landscape is at critical slope (i.e., topographic gradients approaching S_c) and

1416   therefore responds very quickly to changes in channel incision rates, consistent with the

1417   predictions of Mudd and Furbish (2007). Note the noise at slower erosion rates is an

1418   artefact of the adaptive time step of the numerical model.

1419

1420   **Figure 5.** Model predictions of error in estimated transport coefficient (D) given a step

1421   change in this coefficient. The initial and final values of D are denoted by D_i and D_f,

1422   respectively. Panels **a.** and **b.** show two different background erosion rates. The actual

1423   transport coefficient is set within the model. The apparent D is calculated by dividing the

1424   apparent erosion rate, as determined by ^{10}Be in the soil column, by the ridgetop curvature.

1425   Shaded areas represent errors of 10% or less. The noise in the data comes from two

1426   sources: i) curvature is a numerical approximation and ii) apparent erosion rates are

1427   calculated from particles advected toward the surface of the model; the topmost particle

1428   is used to calculate apparent erosion rates using equation (5) but slight errors occur

1429   because the particle is not always located exactly at the surface of the model.

1430

1431 **Figure 6.** Hillslope relaxation time ($4D/(\pi L_H)^2$; Mudd and Furbish, 2007) plotted as a

1432 function of the transport coefficient (D) and hillslope length (L_H).

1433

1434 **Figure 7.** Initial landscapes for the transient landscape simulations. Note the difference

1435 in color scale between the two figures.

1436

1437 **Figure 8.** Apparent and actual erosion rates under different transient scenarios. Actual

1438 erosion rates are the landscape averaged erosion rates from the previous timestep,

1439 whereas the apparent erosion rates are calculated based on simulated concentrations of

1440 [10]Be emerging from the landscape. The entire landscape is eroding, there is no storage

1441 of particles once they are eroded. Variation of forcing parameters has either a 100 kyr

1442 period (a-c; g-i) or 40 kyr period (**d-f**; **j-l**). For varying K and D, the parameters are varied

1443 with amplitude of 0.3 times the mean value.

1444

1445 **Figure 9.** Examples of the spatial distribution of erosion rates for different landscape

1446 evolution scenarios. All simulations have a period of 100 kyr and a K value of 0.00005 yr[-]

1447 [1]. Color scale is the same for all panels. Small plots show the erosion and uplift time

1448 series, and the times of the panels are indicated with vertical dashed black lines. Panels

1449 **a-d** show the simulation that is depicted in Figure 8**g**, and panels **e-h** show the simulation

1450 depicted in Figure 8**f**.

1451

1452   **Figure 10.** An example of disequilibrium χ coordinates across drainage divides near a

1453   channel capture location. The capture point was identified by Harvey and Wells (1987)

1454   near Sorbas, Spain. Catchments with lower χ values are predicted to be 'pushing' the
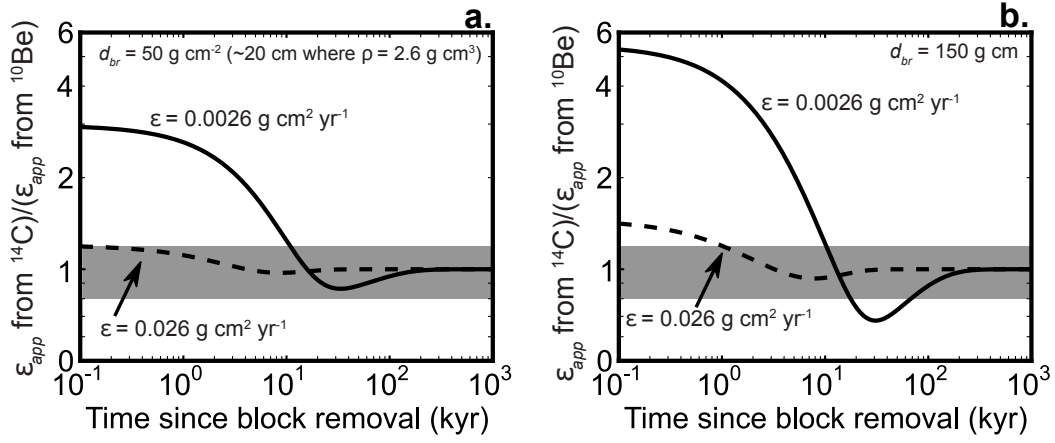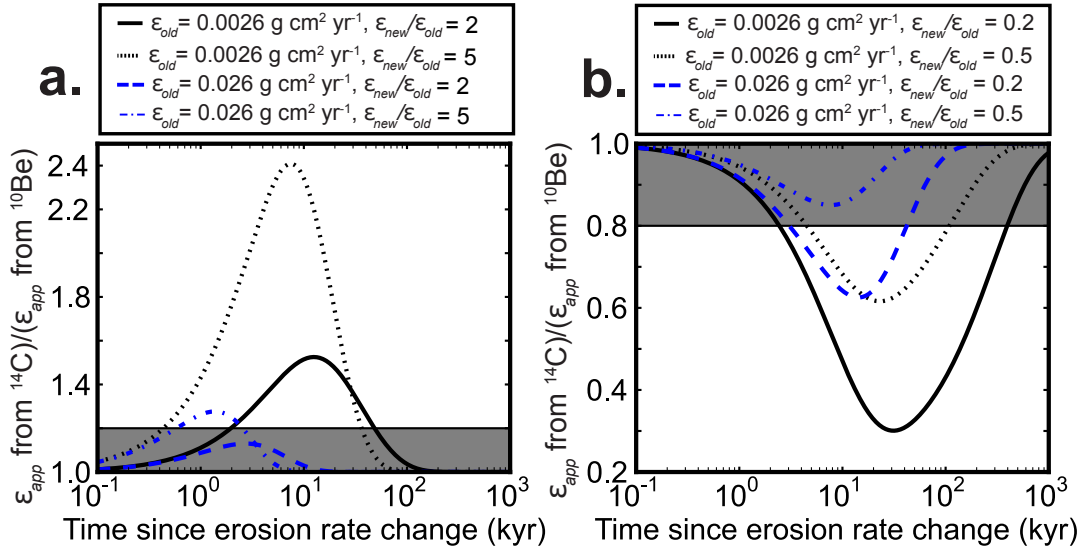
1455   divides toward catchments with higher χ values.

Figure 1: Ratio of the apparent erosion rate calculated from ^{14}C to the apparent erosion rate calculated from ^{10}Be if a block is removed at some time in the past. The depth of block removal (d_{br}) is listed in each panel. The dashed and solid lines in each panel represent different background erosion rates. An erosion rate of 0.0026 g cm^2 yr^{-1} is equivalent to an erosion rate of 0.01 mm yr^{-1} if the rock density is 2.6 g cm^{-1}. The shaded area denotes a 20% difference between erosion rates predicted by in-situ ^{14}C and ^{10}Be; differences below this are likely undetectable.

Figure 2: Ratio of the apparent erosion rate calculated from ^{14}C to the apparent erosion rate calculated from ^{10}Be if there is a step change in erosion rate at some time in the past. Panel **a.** shows scenarios in which erosion rates increase, whereas panel **b.** shows scenarios in which erosion rates decrease. The shaded area denotes a 20% difference between erosion rates predicted by in-situ ^{14}C and ^{10}Be; differences below this are likely undetectable.
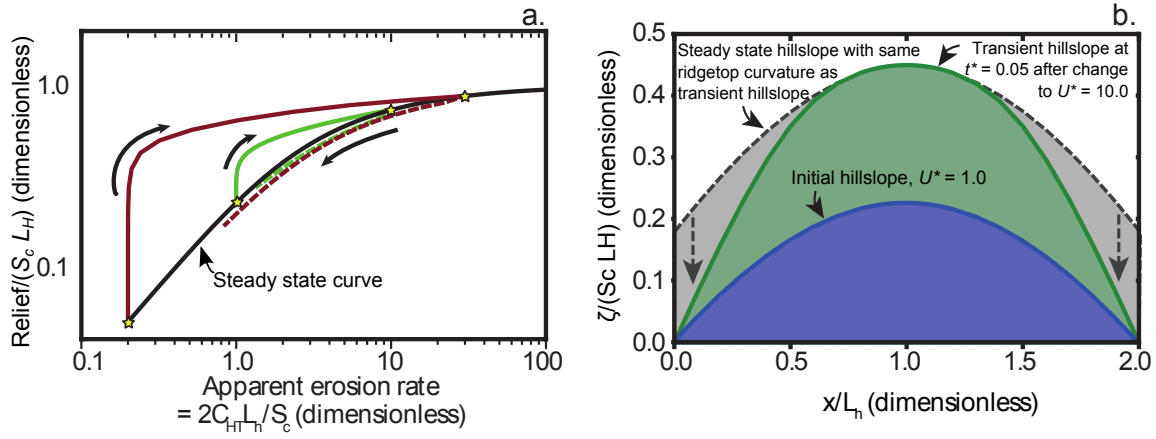
Figure 3: Responses of hillslopes to transient perturbation. Panel **a.** shows in black the curve of dimensionless relief vs dimensionless erosion rate predicted by Roering *et al.*, (2008). The red and green curves show the effect of an increase of erosion rate of two and one orders of magnitude, respectively; stars represent starting and ending positions on the steady state curve. Increased erosion rates result in hillslopes that plot above the steady state curve. Panel **b.** shows a dimensionless hillslope profile. The blue profile is the initial condition, the green curve shows the profile after a dimensionless time (t^*) of 0.05 (that is, after 0.05 times L_H^2/D) following an order of magnitude increase in erosion rate. The dashed grey curve shows a steady state hillslope with the same ridgetop curvature as the green profile, demonstrating that the steady profile has lower relief than the transient profile and illustrating why hillslopes that have increased erosion rates plot above the steady profile in dimensionless relief vs. apparent erosion rate plots.
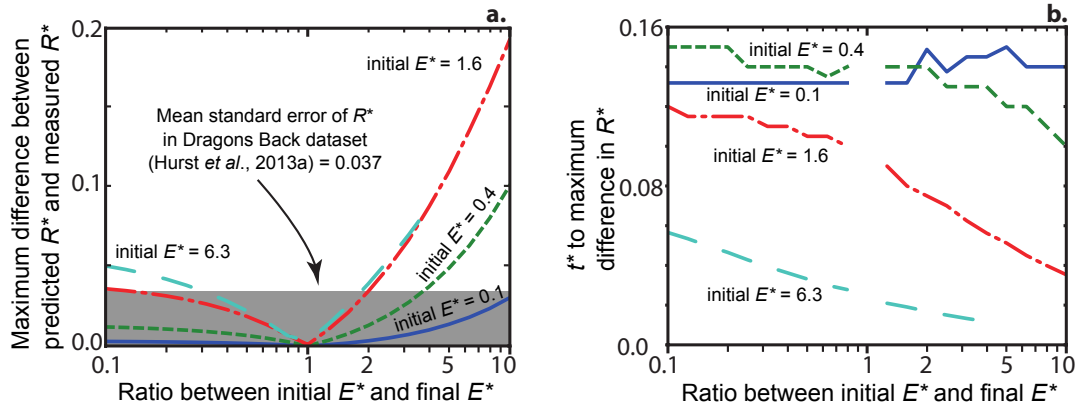
Figure 4: Detection and duration of transience in hillslope profiles in the case of a step change in erosion rate. Panel **a.** shows maximum differences between predicted and measured dimensionless relief (R^*) as a function of both initial erosion rate and the ratio between initial and final erosion rates. Perturbations within the shaded area are unlikely to be detected using E^* vs R^*. The size of the shaded area will depend on the landscape and is determined by the standard error in R^*. Panel **b.** shows the time to the maximum difference in R^*; steeper landscapes (higher E^*) have shorter response times because more of the landscape is at critical slope (i.e., topographic gradients approaching S_c) and therefore responds very quickly to changes in channel incision rates, consistent with the predictions of Mudd and Furbish (2007). Note the noise at slower erosion rates is an artefact of the adaptive time step of the numerical model.
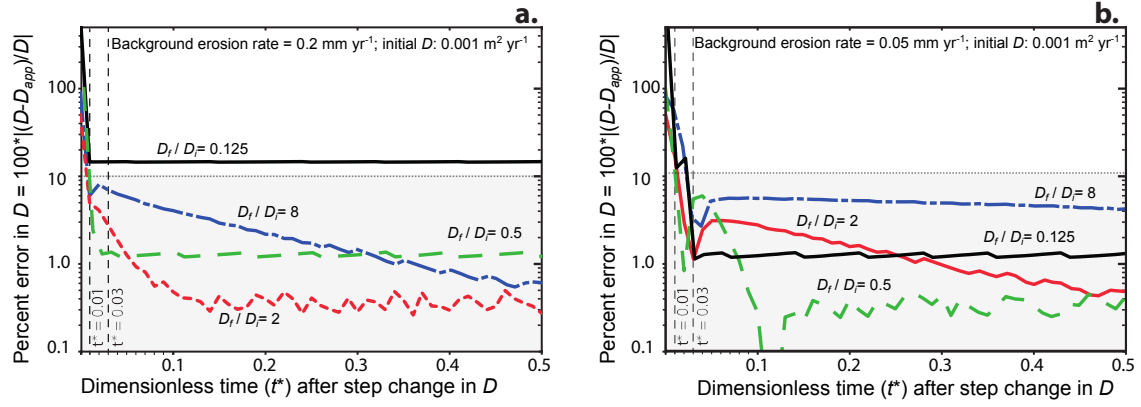
Figure 5: Model predictions of error in estimated transport coefficient (D) given a step change in this coefficient. The initial and final values of D are denoted by D_i and D_f, respectively. Panels **a.** and **b.** show two different background erosion rates. The actual transport coefficient is set within the model. The apparent D is calculated by dividing the apparent erosion rate, as determined by ^{10}Be in the soil column, by the ridgetop curvature. Shaded areas represent errors of 10% or less. The noise in the data comes from two sources: i) curvature is a numerical approximation and ii) apparent erosion rates are calculated from particles advected toward the surface of the model; the topmost particle is used to calculate apparent erosion rates using equation (5) but slight errors occur because the particle is not always located exactly at the surface of the model.
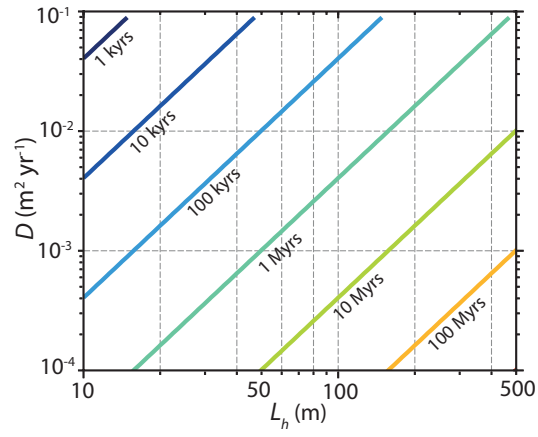
Figure 6: Hillslope relaxation time $(4D/(\pi L_H)^2$; Mudd and Furbish, 2007) plotted as a function of the transport coefficient (D) and hillslope length (L_H).
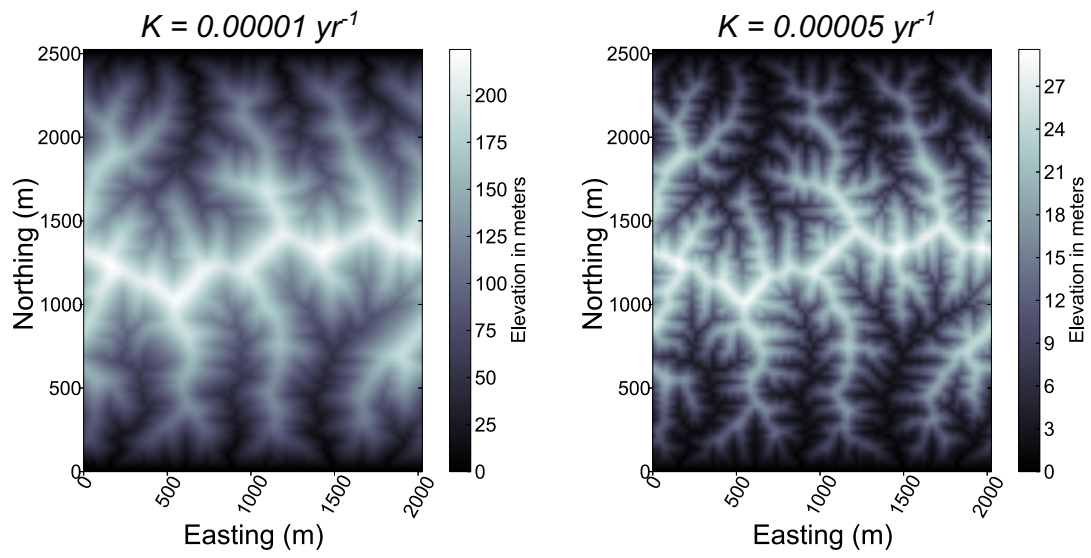
Figure 7: Initial landscapes for the transient landscape simulations. Note the difference in color scale between the two figures.
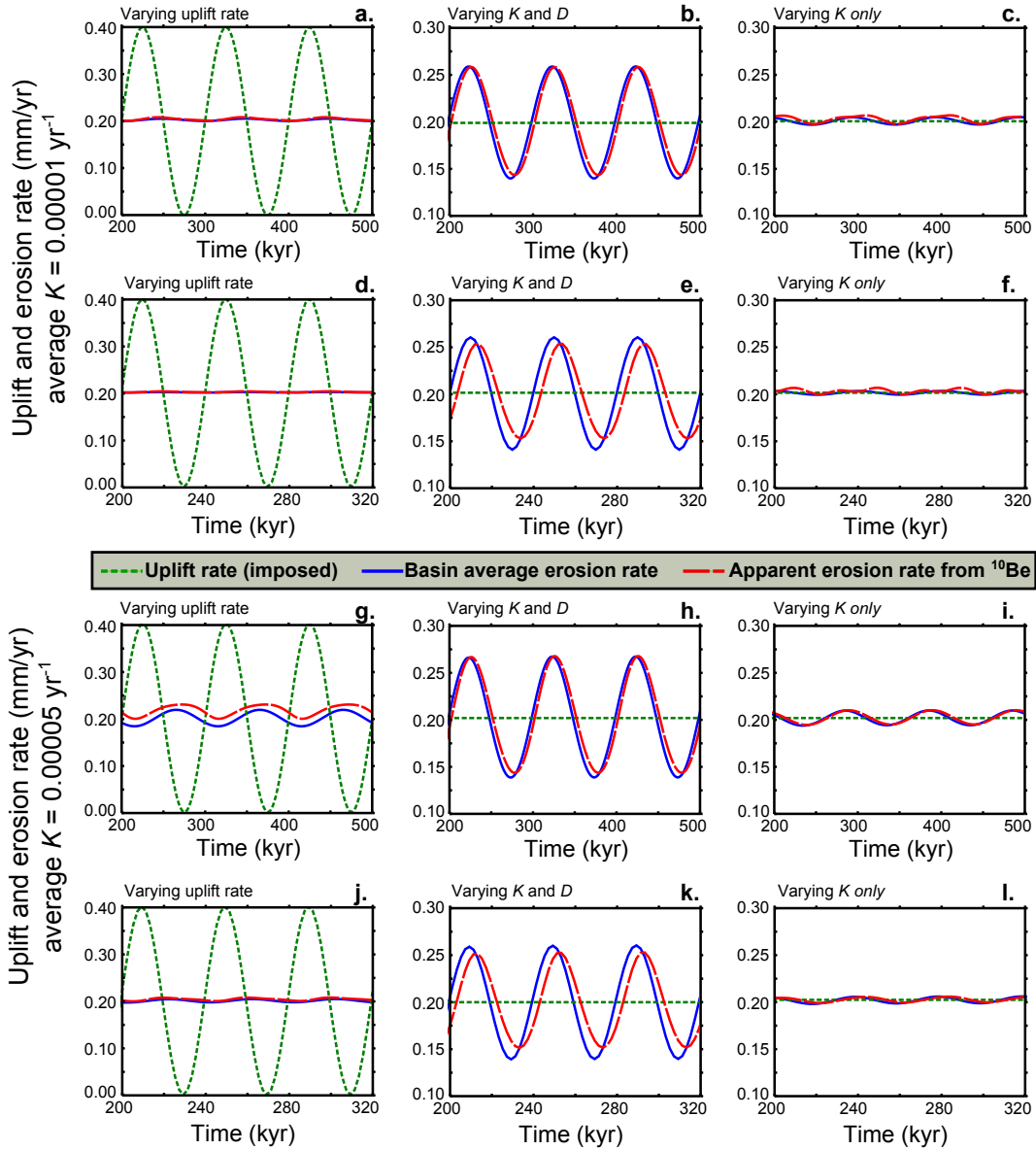
Figure 8: Apparent and actual erosion rates under different transient scenarios. Actual erosion rates are the landscape averaged erosion rates from the previous timestep, whereas the apparent erosion rates are calculated based on simulated concentrations of [10]Be emerging from the landscape. The entire landscape is eroding, there is no storage of particles once they are eroded. Variation of forcing parameters has either a 100 kyr period (**a-c**; **g-i**) or 40 kyr period (**d-f**; **j-l**). For varying K and D, the parameters are varied with amplitude of 0.3 times the mean value.
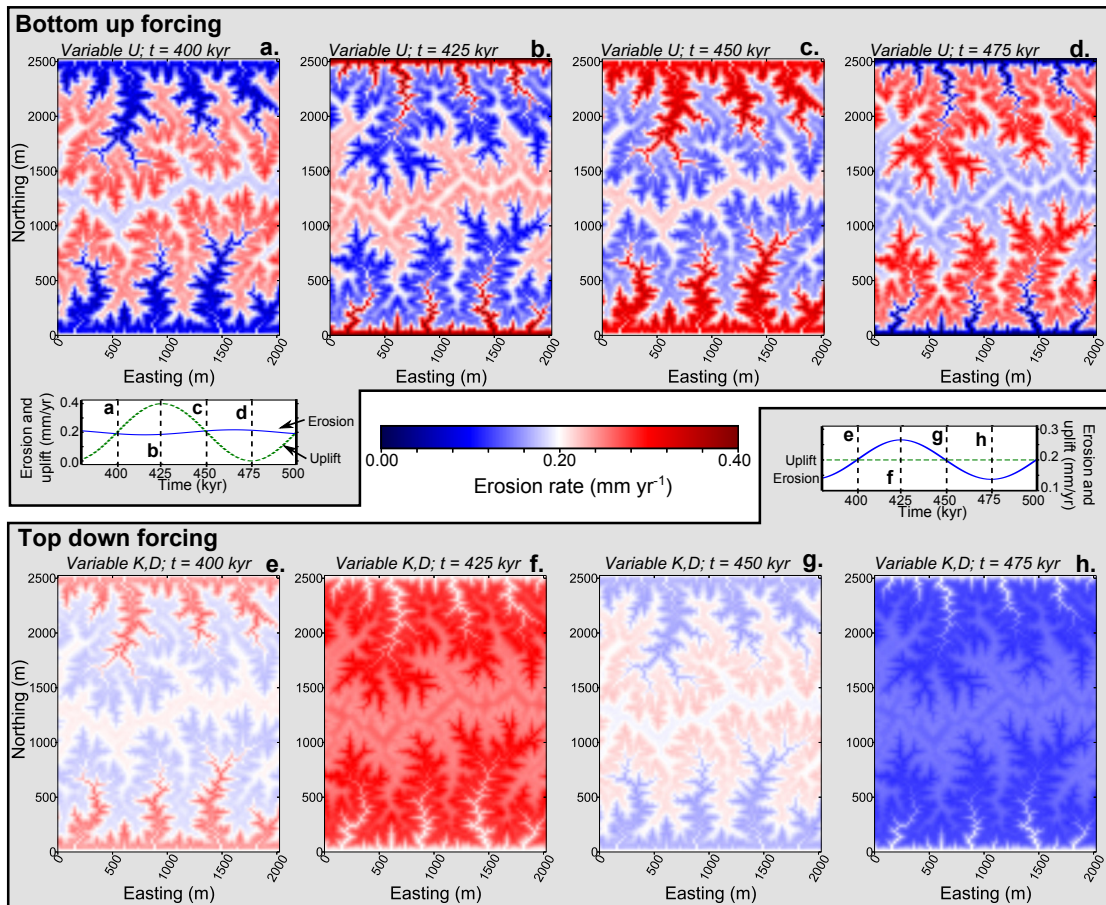
Figure 9: Examples of the spatial distribution of erosion rates for different landscape evolution scenarios. All simulations have a period of 100 kyr and a K value of 0.00005 yr^{-1}. Color scale is the same for all panels. Small plots show the erosion and uplift time series, and the times of the panels are indicated with vertical dashed black lines. Panels a-d show the simulation that is depicted in Figure 8g, and panels e-h show the simulation depicted in Figure 8f.
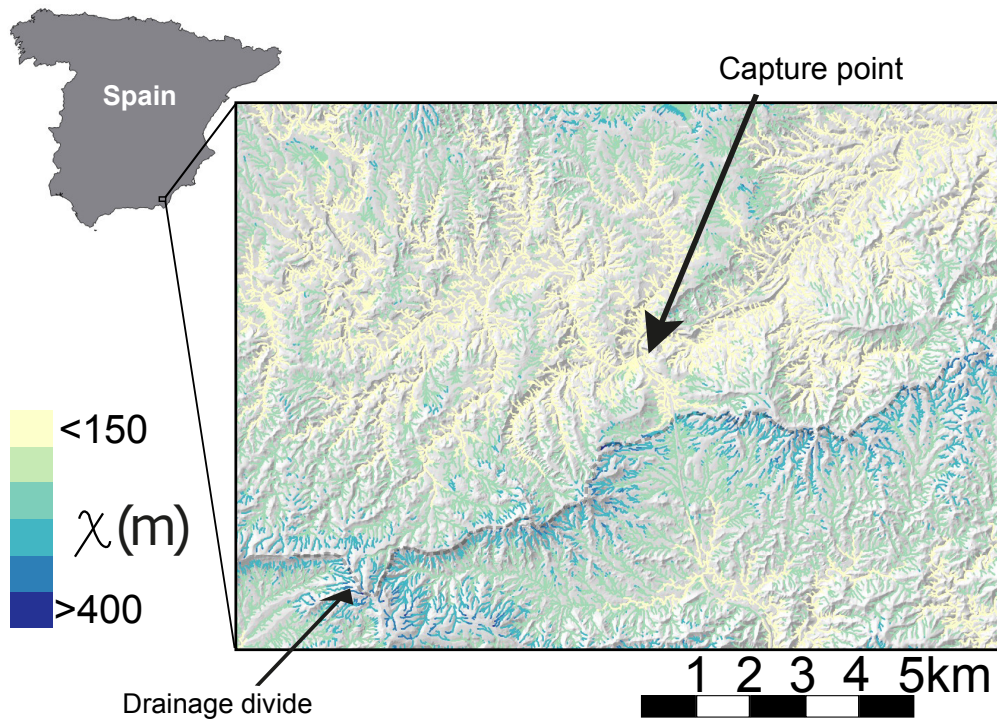
Figure 10: An example of disequilibrium χ coordinates across drainage divides near a channel capture location. The capture point was identified by Harvey and Wells (1987) near Sorbas, Spain. Catchments with lower χ values are predicted to be pushing the divides toward catchments with higher χ values.